Materials & Design 265 (2026) 115924

Contents lists available at ScienceDirect

Materials & Design

journal homepage: www.elsevier.com/locate/matdes

Spatiotemporal multi-sensor characterization of melt pool dynamics in laser directed energy deposition

Gen Tian [a], Yang Zhao [a], Wenyu Wang [a], Guofeng Han [a], Zhiqiang Ren [a], Xiaoming Wang [a,*], Lu Lu [b,*], Sheng Zhu [a]

[a] National Key Laboratory for Remanufacturing, Army Arms University of PLA, Beijing 100072, China
[b] Southwest Jiaotong University School of Mechanical Engineering, Chengdu 610031, China

ARTICLE INFO

Keywords:
Laser powder directed energy deposition
Multi-sensor fusion
Spatiotemporal correlation analysis
Melt pool monitoring
Process optimization

ABSTRACT

Laser directed energy deposition (L-DED) technology has gained significant attention for its potential in manufacturing complex components. However, its industrial adoption is constrained by process fluctuations that cause variability in quality and mechanical properties. To address this challenge, a robot-assisted multi-sensor monitoring system (CMOS camera, NIR camera, microphone, and spectrometer) is developed, together with a software architecture for synchronized acquisition of heterogeneous signals. The key novelty of this research is a spatiotemporal feature fusion framework that enables mining of process data and comprehensive analysis of melt pool dynamic evolution. Correlation analysis is employed to elucidate the coupling mechanisms among multi-sensor signals, identifying key features and eliminating redundancies. The effects of laser scanning speed and power on melt pool geometry, temperature distribution, reaction intensity, and elemental excitation states are investigated, leading to quantitative correlations between process parameters and critical signal characteristics. The influence of process parameters on forming quality is assessed by scoring the single-bead deposits, from which a stable process window is established. This work reveals the quantitative relationships among process parameters, multi-sensor signal features, and L-DED formation quality. The findings provide prior knowledge for in-situ monitoring and future closed-loop control of the L-DED process.

1. Introduction

Metal additive manufacturing has emerged as a key pillar of advanced manufacturing, offering capabilities for fabricating geometrically complex, lightweight structures with shortened product development cycles, and superior mechanical properties [1–3]. In particular, laser-directed energy deposition (L-DED) has been extensively adopted for the integrated manufacturing of large, intricate components in sectors such as aerospace, energy and power, and rail transportation. Nevertheless, maintaining consistently high process stability and quality uniformity remains a critical challenge for L-DED technology. Even with pre-optimized process parameters, the interplay of factors including non-uniform energy distribution, variations in powder particle size, and gas entrapment can lead to significant melt pool fluctuations, localized inhomogeneous heat accumulation, and insufficient material melting [4–7]. During the fabrication process, these instabilities can subsequently induce defects such as porosity and cracks, which severely compromise the mechanical performance of the final parts. Consequently, in-situ online monitoring and closed-loop control of the geometry, temperature gradient, reaction intensity, and material excitation state during L-DED are essential for the timely prediction and prevention of defects.

In recent years, academia and industry have devoted significant efforts into online monitoring for metal additive manufacturing. Predominant approaches utilize visual cameras, infrared thermal sensors, microphones, and optical spectrometers to capture melt pool visual images, infrared images, acoustic signals, and plasma spectra. These data are subsequently integrated with signal processing techniques or machine learning models to facilitate online monitoring of dynamic melt pool characteristics and defect prediction. For instance, Perani[8] et al. employed melt pool images and process parameters to predict part dimensional accuracy. Oster[9] et al. utilized thermal signatures and X-ray computed tomography data to forecast localized porosity within sub-volumes. Chen[10,11] et al. predicted keyhole and crack defects during

* Corresponding authors.
E-mail addresses: uwangxm@126.com (X. Wang), lulu@swjtu.edu.cn (L. Lu).

https://doi.org/10.1016/j.matdes.2026.115924
Received 12 January 2026; Received in revised form 12 March 2026; Accepted 25 March 2026
Available online 29 March 2026

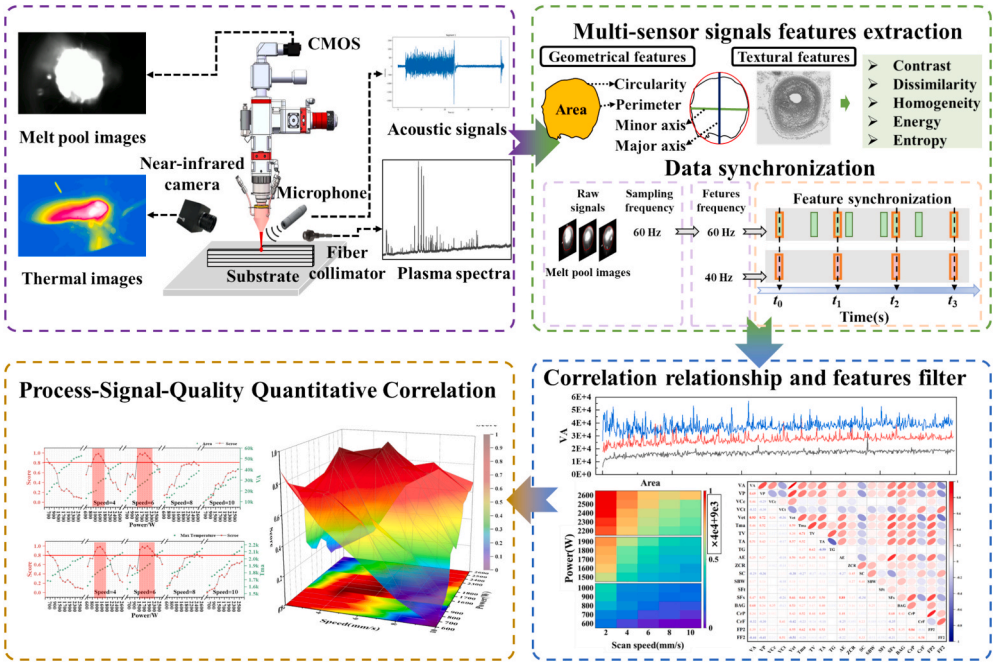

Fig. 1. Methodological framework for establishing quantitative relationships among process parameters, multi-modal signals, and forming quality based on multi-sensor fusion and spatiotemporal correlation analysis.

the L-DED process through acoustic signals. Squires[12] et al. employed laser-induced breakdown spectroscopy for composition monitoring during directed energy deposition of gradient iron-nickel alloys. Although these methods have achieved significant results in online monitoring of melt pool features and defect prediction, the formation of pore and crack defects is comprehensively influenced by a combination of factors, including melt pool geometric features, temperature distribution, reaction intensity, and plasma excitation degree. Therefore, monitoring techniques relying on a single sensor are often inadequate for achieving comprehensive, robust online process monitoring and accurate defect prediction [13,14]. To address this challenge, multi-sensor monitoring technology has emerged, which not only compensates for the constraints of individual sensors but also provides a foundation for more reliable and robust defect prediction.

In the field of laser additive manufacturing, multi-sensor monitoring and data fusion technologies have established a foundational research base [14–16]. Wu[17] et al. proposed an in-situ quality classification method for the laser powder bed fusion (LPBF) process based on a multi-sensor fusion melt pool monitoring system. Gaikwad[18] et al. developed a system incorporating a high-speed camera and melt pool temperature imaging system to acquire LPBF process monitoring data, demonstrating that utilizing multiple monitoring data significantly improved predictions of process anomalies and defect formation. Montazeri[19] et al. employed data from spectrometers and optical cameras to capture dynamic phenomena around the melt pool region. Compared with traditional single-sensor monitoring technology, multi-sensor monitoring methods can achieve comprehensive process monitoring and high-precision defect prediction. Chen[20] et al. developed a multi-sensor fusion digital twin framework, achieving high-precision prediction and prior intervention of internal pore defects in L-DED components, realizing proof-of-concept for this technology. However, due to the lack of spatiotemporal fusion analysis methods capable of quantifying the tight coupling relationship among process parameters, multi-modal signals, and forming quality, closed-loop control technology based on multi-sensor fusion to achieve online suppression of internal defects in L-DED components remains to be explored.

This work presents a systematic methodology based on multi-sensor fusion and spatiotemporal correlation analysis to elucidate the dynamic evolution patterns of the melt pool in the laser-directed energy deposition process and to establish quantitative relationships among process parameters, multi-modal signals, and forming quality. The principal innovations of this work are threefold. First, key signal features are extracted from each sensor stream by analyzing the Pearson correlation coefficients among the multi-sensor signals. Second, the correlations between laser power/scanning speed and these key signal features are investigated, revealing their influence on melt pool geometry, temperature field, reaction intensity, and elemental excitation states. Third, the L-DED process window is identified by analyzing the influence patterns of process parameters on deposit geometric morphology. A quantitative model relating process parameters, multi-modal signals, and forming quality is established by integrating the identified process window with the aforementioned correlations. This model explicitly defines the appropriate ranges for multi-source signal characteristic values, providing a critical foundation for effective online monitoring of the L-DED process.

2. Overview of the framework

Fig. 1 illustrates the proposed method based on multi-sensor fusion and spatiotemporal correlation analysis for quantifying the relationships among process parameters, multi-modal signals, and forming quality. The framework primarily consists of the following three steps.

(1) System Development: A robot-assisted, multi-sensor integrated L-DED additive manufacturing system was developed. This system incorporates four types of sensors: a coaxial CMOS camera, a near-infrared camera, a microphone, and a spectrometer, enabling the synchronous in-situ acquisition of visual images, infrared images, acoustic signals, and plasma spectral signals from the melt pool. The detailed hardware architecture and software framework of the system are described in Section 3.1.

(2) Feature Extraction and Correlation Analysis: Image processing and signal analysis techniques were employed to extract time-domain feature values from visual images, infrared images, acoustic signals, and plasma spectral signals. Subsequently, a spatiotemporal fusion analysis was conducted on the features

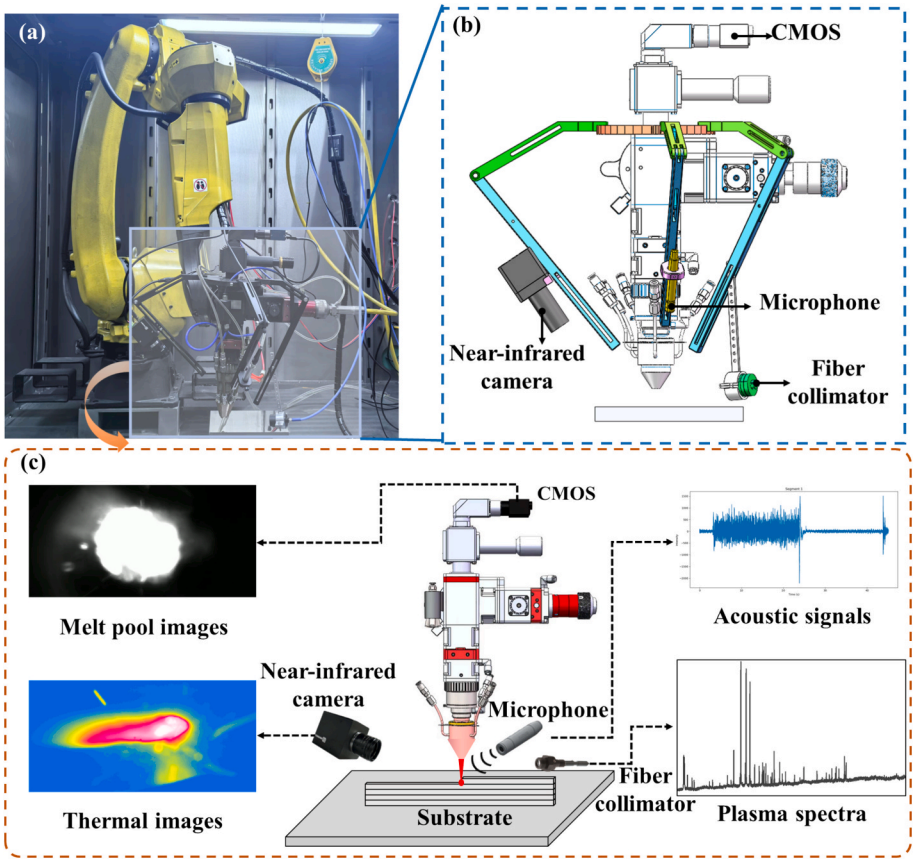

Fig. 2. Experimental setup and schematic diagrams: (a) Robotic laser-directed energy deposition system; (b) In-situ integration of multi-sensors, including a microphone, a coaxial CMOS camera, a fiber collimator, and a near IR camera; (c) Schematic diagram of co-axial and off-axial sensing process in robotic L-DED.

from the four signal types to identify the key characteristics and to elucidate the influence patterns of laser scanning speed and power on melt pool geometric morphology, temperature distribution, reaction intensity, and element excitation state. This step clarifies the intrinsic correlations between process parameters and key signal features, laying the groundwork for establishing the subsequent quantitative model.

(3) Process Window Identification and Quantitative Model Establishment: The influence of process parameters on L-DED forming quality was systematically investigated by extracting the geometrical dimensions of single-bead deposits under different parameter combinations, leading to the definition of a stable process window. Finally, quantitative relationships among "process parameters—multi-modal signals—forming quality" were established by integrating the correlation analysis between process parameters and key signal features with the identified process window. This model defines the appropriate operating ranges for multi-source signal characteristics, providing explicit feedback criteria for closed-loop control strategies.

3. Experimental setup and methodology

3.1. System setup

An integrated in-situ multi-sensor system was developed for the real-time monitoring of the robotic L-DED process, with the overall configuration illustrated in Fig. 2(a). For the robotic L-DED process, a 6-axis industrial robot carried a coaxial powder-blown nozzle. A melt pool is formed as metal powder is injected into the substrate and melted by a 1080 nm wavelength laser beam. Four types of sensors were integrated, including a CMOS camera, a Near-Infrared (NIR) camera, a microphone, and an optical spectrometer.

The CMOS camera is coaxially aligned with the laser optical system for online capture of melt pool images. The NIR camera is installed at a 45° angle and 250 mm away from the melt pool to effectively acquire thermal images. Acoustic signals are acquired using a microphone installed at a 45° angle and 200 mm away from the melt pool relative to the laser head to minimize interference from the laser system. The plasma emission spectra are recorded using an optical spectrometer, as

Table 1
Models and parameters of main equipment.

No.	Name	Model	Function	Main Parameters	Manufacturer
1	CMOS	MER2-160-75GM	Coaxial collection of molten pool images	Resolution: 1440 × 1080; Frame rate: 300 fps	Daheng Imaging Technology Co., Ltd
2	NIR Camera	MAGNITY HT60	Collection of molten pool temperature fields	Wavelength: 0.9-1.1 umμm; Pixel count: 640 × 480; Frame rate: 50 Hz; Temperature range: 600–2500℃	MAGNITY Electronics Co., Ltd.
3	Spectrometer	AvaSpec-ULS4096CL-EVO	Plasma spectrum collection	Resolution: 0.05–20 nm; Wavelength range: 200–1100 nm; Sampling rate: 0.70 ms/scan	Avantes B.V.
4	Microphone	MPA201	Deposition sound collection	Sensitivity (@250 Hz): 50 mV/Pa (−26 dB re 1 V/Pa); Frequency response: 10 Hz ~ 20 kHz (±2 dB); Dynamic range: 17 dBA ~ 135 dB	BSWA TECHNOLOGY CO., LTD

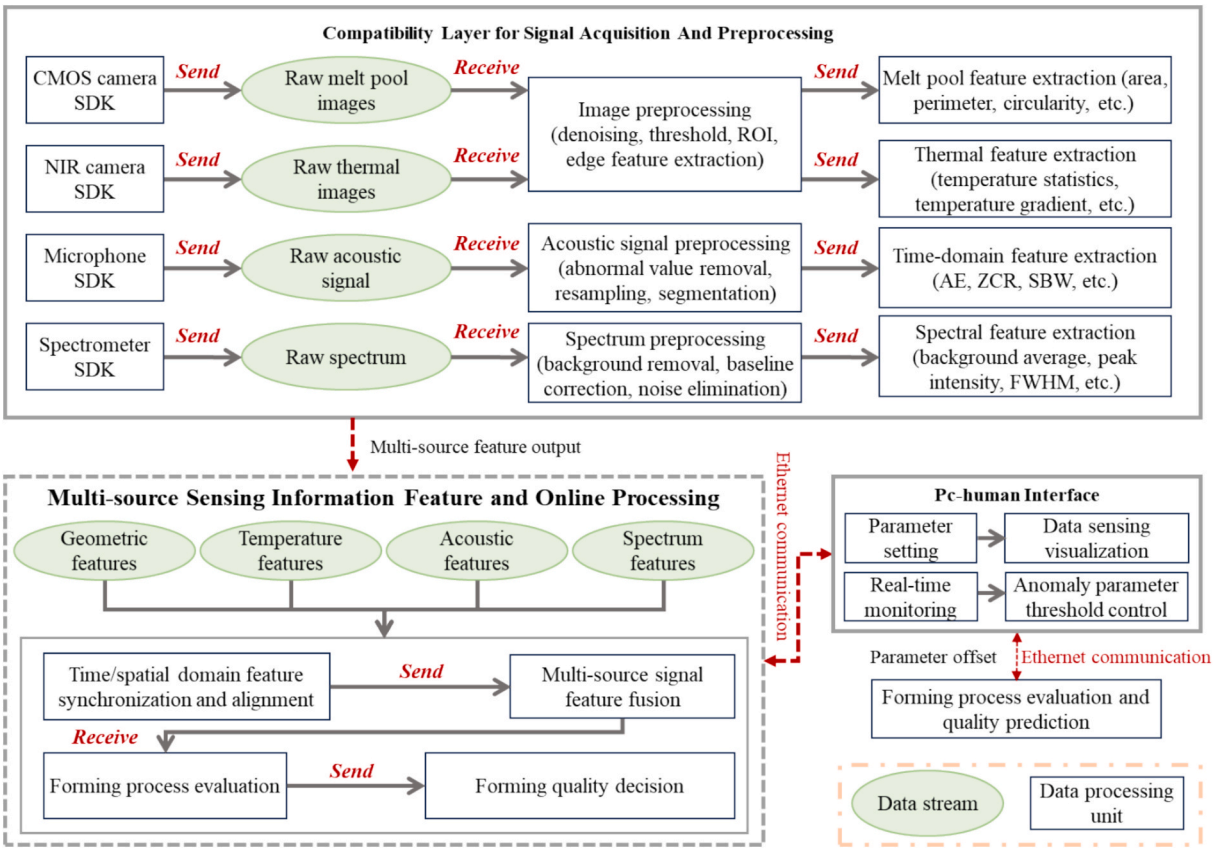

Fig. 3. Software architecture of the multi-sensors monitoring system.

Table 2
Chemical composition (wt%) of 316 L steel powder.

Element(wt.%)	Fe	Ni	Si	Cr	Mn	Mo	C	P	S
	bal.	11.28	0.37	16.68	1.11	2.66	0.013	0.024	<0.003

depicted in Fig. 2(c). The models and key parameters of the primary equipment in the multi-sensor system are listed in Table 1.

A software architecture for the multi-sensor system was developed to elucidate the underlying process mechanisms and accurately monitor melt pool evolution. As shown in Fig. 3, multi-sensing signals are synchronized by establishing a unified timestamp. A compatibility module was designed to decode heterogeneous signals into standardized numerical formats, addressing challenges such as data desynchronization, high-frequency data storage limitations, and suboptimal human–machine interaction.

The system integrates heterogeneous sensors through a compatibility layer, unifying interfaces, communication protocols, data structures, and operational logic. The adoption of a layered architecture comprising a graphical user interface (GUI), an intermediate compatibility layer, and a service and storage layer, the design reduces system complexity and enhances operational efficiency and stability. A global unified timestamp synchronization mechanism resolves sensor synchronization issues, while a data buffer pool ensures real-time storage and prevents data loss, improving collection efficiency. The GUI, developed using the PyQt framework, provides an intuitive real-time sensor parameter adjustments, status monitoring, and data visualization. This system optimizes data collection, storage integrity, and user interaction, providing a reliable solution for complex multi-source perception applications.

Table 3
Physical properties of 316 L steel powder.

Particle Size Distribution(μm)			Hall Flow Rate(s/50 g)	Bulk Density(g/cm^3)	Tap Density(g/cm^3)
D10	D50	D90	16.2	4.12	4.9
49.7	71.0	99.7			

3.2. Experiment

Commercially available 316 L stainless steel powder produced by vacuum atomization was used in the L-DED experiments. Its chemical composition and primary physical properties are listed in Table 2 and Table 3, respectively. A homogeneous steel plate with the same elemental composition as the powder, measuring 200 × 150 × 16 mm, served as the substrate. Prior to deposition, the substrate surface was polished, subsequently cleaned with anhydrous ethanol, and dried using compressed air.

During the deposition experiments, the laser power was categorized into low, medium, and high ranges, as illustrated in Fig. 4. The range of 600–1000 W was defined as low power, 1500–1900 W as medium power, and 2200–2600 W as high power. Within each laser power range, the scanning speed was set to 2, 4, 6, 8, and 10 mm/s, respectively, while maintaining a constant powder feed rate of 1 rad/min. The combinations of process parameters are listed in Table 4.

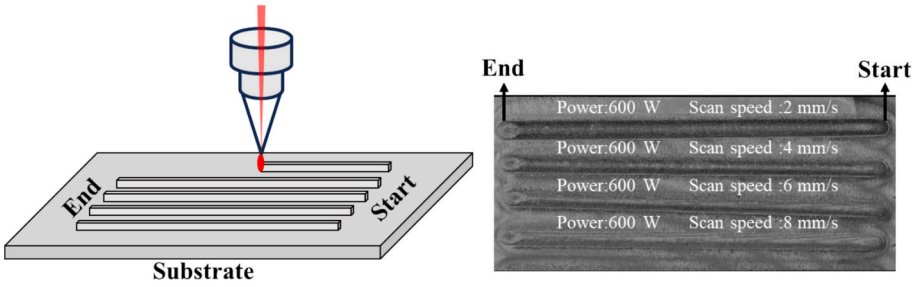

Fig. 4. Deposition strategy.

Table 4
L-DED experiment parameters.

	Laser power (W)	Scan speed (mm/s)	Feeding rate (rad/min)
Low	600–1000 (100)	2 4 6 8 10	1
Medium	1500–1900 (100)		
High	2200–2600 (100)		

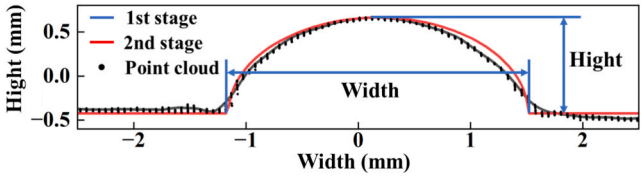

Fig. 5. Schematic diagram of the formed width and height extraction process.

Following the deposition process, it is essential to evaluate the surface morphology of the clad, as the bead geometry directly determines the forming accuracy and surface quality of the cladding layer. The geometric characteristics of a single track, particularly bead width and height, are critical quality indicators that significantly influence the quality of the final part [21,22]. The surface morphology was assessed using the point cloud obtained from a UC3D line laser profilometer. The principal axis direction of the point cloud was determined via Principal Component Analysis (PCA) to identify the deposition direction. The entire clad track was divided into 200 cross-sections at equal intervals along this deposition direction. For each cross-section, a fractal statistical method was employed to extract the upper profile of the cross-section. Specifically, cross-sectional points were dynamically partitioned into 20 to 100 bins along the width direction, and the 90th percentile of height values in each bin was taken as the contour point at that position. Compared to directly using the maximum value, this percentile method is more effective in suppressing the influence of measurement noise.

Contour fitting was performed in two stages. In the first stage, a PCHIP was used to generate a fine-fitted curve with 500 points. This method preserves data monotonicity and avoids the Runge's phenomenon common in high-order polynomial fitting. Subsequently, a third-order Savitzky-Golay filter with a suitable window length was applied for further smoothing. Potential oscillations were detected by monitoring sign changes in the second derivative. If the number of oscillations exceeded 30% of the total points, additional moving average processing was applied. In the second stage, an idealized contour was generated based on the fine curve. The substrate height was determined from the median height in the edge regions. Clad boundaries were identified by searching bilaterally from the highest point using criteria combining a threshold of 15% of the maximum height and a maximum derivative of 5%. Finally, an idealized model of "straight line-semi-ellipse-straight line" was constructed, where the semi-ellipse part describes the geometric characteristics of the cladding region. The overall processing workflow is depicted in Fig. 5.

3.3. Multi-sensor signals features extraction

3.3.1. Coaxial visible camera melt pool images

Features were extracted from visible melt pool images captured by a CMOS camera, as shown in Fig. 6. The raw images were enhanced using Gaussian blur [23] and Contrast Limited Adaptive Histogram Equalization (CLAHE) [24]. As shown in Fig. 6(a), the contours of the molten pool were extracted using the Suzuki-Abe algorithm [25]. The melt pool area was calculated by counting pixels enclosed within the contours, and the perimeter was determined by accumulating the Euclidean distances between adjacent pixels along the contour [26]. The circularity was

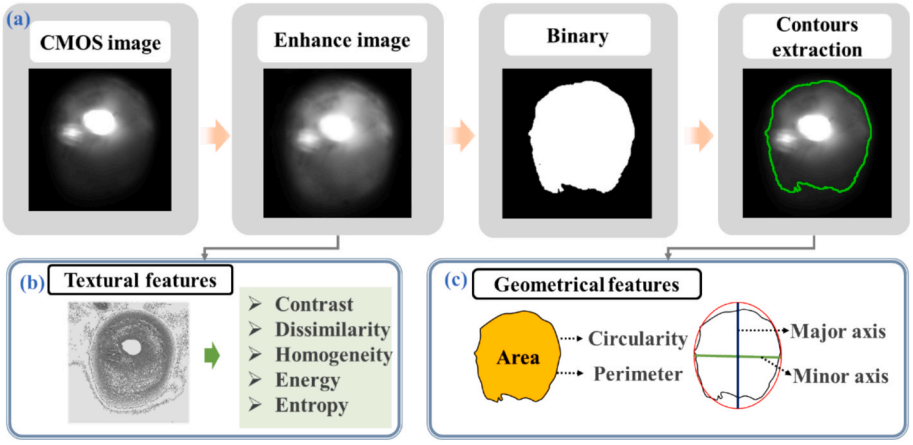

Fig. 6. Schematic diagram of melt pool feature extraction: (a) morphological processing; (b) texture feature extraction; (c) geometric and frequency domain feature extraction.

Table 5
Mathematical definitions and descriptions of visible light image features.

Num.	Type		Formula	Description
1	Area		$VA = \sum_{x,y} I(x,y)$	Number of pixels inside the contour
2	Perimeter		$VP = \sum_{i=1}^{N} \sqrt{(x_{i+1}-x_i)^2 + (y_{i+1}-y_i)^2}$	Total length of the contour's boundary
3	Circularity		$VC = 4\pi \times \text{Area}/VP^2$	Measures how closely the shape resembles a circle
4	Major Axis Length		$\frac{(x\cos\alpha + y\sin\alpha)^2}{a^2} + \frac{(x\sin\alpha - y\cos\alpha)^2}{b^2} = 1 VMa = \max(a,b),\ VMi = \min(a,b)$	Fits an ellipse and extracts the major and minor axes
5	Minor Axis Length			
6	GLCM	Contrast	$VC = \sum_{i,j} P(i,j)(i-j)^2$	Measures gray-level variation
7		Dissimilarity	$VD = \sum_{i,j} P(i,j)\lvert i-j\rvert$	Average absolute difference of gray values
8		Homogeneity	$VH = \sum_{i,j} P(i,j)/(1+(i-j)^2)$	Normalized sum of the matrix
9		Energy	$VEe = \sqrt{\sum_{i,j} P(i,j)^2}$	Normalized sum of squared elements
10		Shannon Entropy	$VEt = -\sum_i p_i \log(p_i).$	Measures the information content or complexity of the image

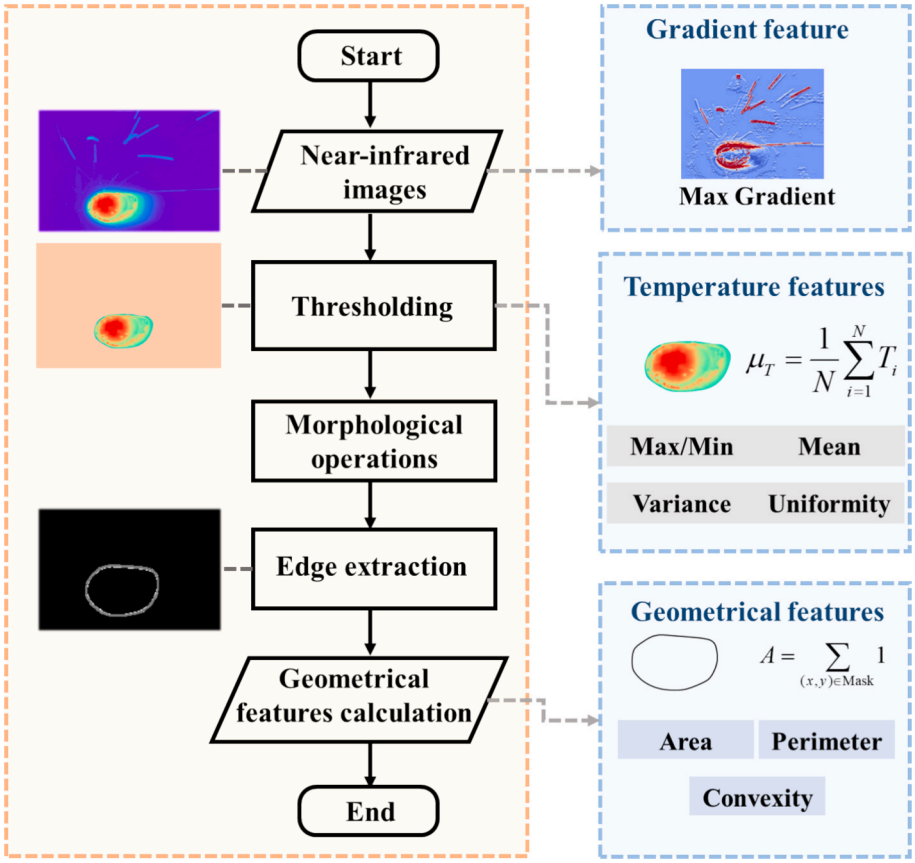

Fig. 7. Temperature field feature extraction.

evaluated using Equation (3) (Table 5). The major and minor axis lengths were obtained by fitting an ellipse to the molten pool contour, as shown in Fig. 6(c).

A region of interest (ROI) was cropped from the raw image, as presented in Fig. 6(b). The gray-level co-occurrence matrix of the ROI was computed to derive textural metrics—contrast, dissimilarity, homogeneity, and energy. Entropy, calculated using Equation (10), was introduced to evaluate the complexity of surface fluctuations during deposition.

3.3.2. *Off-axis thermal melt pool images*

Thermal images of the molten pool were captured using an NIR camera, as shown in Fig. 7. Gradient features in multiple orientations were calculated using Equation (8) (Table 6). A fixed threshold of 1500 ℃ was applied to identify the ROI. Time-domain feature values including maximum, minimum, mean, variance, and uniformity factor were extracted from these ROI to characterize the thermal state of the molten pool. Moreover, the edges of the temperature fields were extracted using morphological operations. Geometrical features including area, perimeter, compactness, and convexity were then calculated to reveal the morphology of the molten pool. The mathematical definitions and descriptions of temperature field features are provided in Table 6.

3.3.3. *In-situ acoustic signals*

Low-frequency acoustic signals serve as critical indicators of laser-material interaction dynamics and defect formation during the AM process [27]. As illustrated in Fig. 8, the acoustic signals were acquired by a microphone at a sampling rate of 44.1 kHz. Audio equalization was applied to suppress low-frequency noise, followed by a 3–21 kHz

Table 6
Mathematical definitions and descriptions of infrared temperature field features.

Num.	Name	Formula	Description
1	Mean Temperature	$\mathrm{Tme} = \frac{1}{N}\sum_{i=1}^{N} T_i$	Reflects the overall thermal state of the molten pool.
2	Maximum and Minimum Temperature	$\mathrm{Tma} = \max(T_i), \quad \mathrm{Tmi} = \min(T_i)$	The highest and lowest temperatures within the molten pool.
3	Temperature Variance	$\mathrm{TV} = \frac{1}{N}\sum_{i=1}^{N}(T_i - \mu_T)^2,$	Indicates the degree of temperature fluctuation.
4	Temperature Uniformity	$\mathrm{TU} = 1 - \frac{\sigma_T^2}{\mu_T}$	Measures the uniformity of temperature distribution in the molten pool.
5	Area	$\mathrm{TA} = \sum_{(x,y)\in\Omega} \mathbf{1}_{T(x,y)\geq Threshold},$	The area of the molten pool region, measured in pixels.
6	Perimeter	$\mathrm{TP} = \sum_{i=1}^{N}\sqrt{(x_{i+1}-x_i)^2 + (y_{i+1}-y_i)^2}$	The perimeter of the molten pool region.
7	Convexity	$\mathrm{TC} = \frac{A_{\mathrm{convex}}}{A_{\mathrm{pool}}}, \quad A_{\mathrm{pool}} > 0$	Reflects the similarity of the molten pool shape to its convex hull.
8	Max Gradient	$\mathrm{TG} = \frac{1}{\lvert\Omega\rvert}\underset{(x,y)\in\Omega}{\mathrm{Max}}\sqrt{\left(\frac{\partial T}{\partial x}\right)^2 + \left(\frac{\partial T}{\partial y}\right)^2 + \left(\frac{\partial T}{\partial x \partial y}\right)^2 + \left(-\frac{\partial T}{\partial x \partial y}\right)^2}$	Reflects the max rate of temperature change.

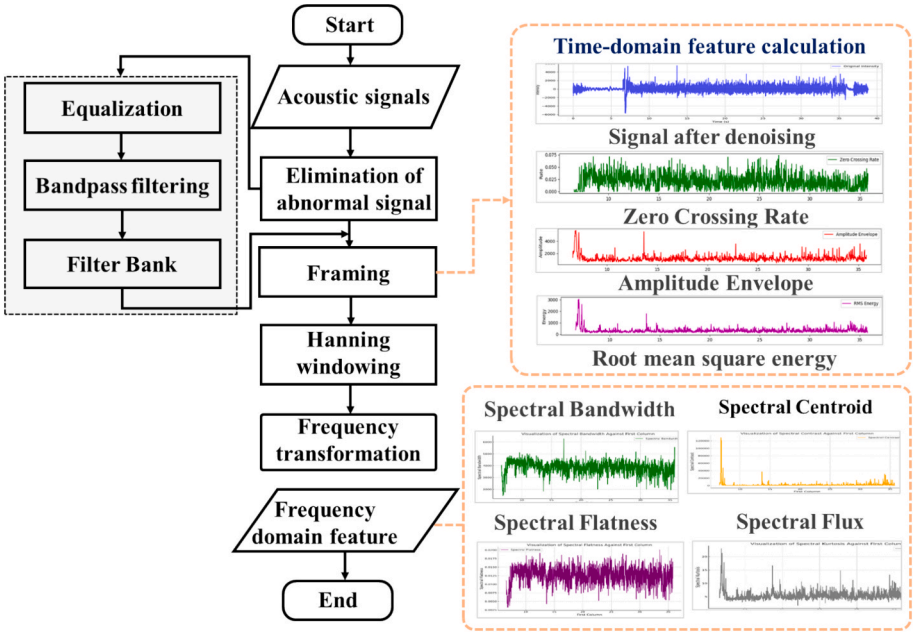

Fig. 8. Flowchart for the acoustic signal feature extraction.

bandpass filter to eliminate out-of-band noise. Harmonic-percussive source separation was further employed to enhance the acquired signals [11]. The denoised signals were segmented into frames for time-domain feature extraction, as shown in Fig. 8(a). The zero-crossing rate represents the degree of material melting during the process, while the amplitude envelope and RMS values indicate the energy intensity. Furthermore, when converting the time-domain acoustic signals to the frequency domain using FFT, a Hanning window was utilized to prevent spectral leakage. Frequency-domain features, including spectral bandwidth, spectral contrast, spectral flatness, and spectral kurtosis, were then extracted. The mathematical definitions of the acoustic features in both time and frequency domains are provided in Table 7.

3.3.4. *In-situ plasma spectral signals*

The optical spectrometer capable of in situ capturing plasma spectra, providing effective signals for real-time monitoring of the thermodynamic behavior and energy coupling efficiency. As shown in Fig. 9, the double envelope method (DEM) was applied to the original spectral signals through two iterations of lower envelope fitting [28], thereby extracting the background spectrum. Baseline drift and noise were then removed by subtracting the background spectrum from the original spectrum. Subsequently, time-domain features of the processed spectral signals were computed as key indicators for process monitoring. The mathematical definitions of these time-domain spectral features are summarized in Table 8.

3.4. *Data synchronization and correlation analysis*

A data synchronization and fusion method based on temporal alignment and unified resampling was developed to address the challenges of sampling frequency discrepancies and initialization time offsets in multi-sensor signal acquisition. The multi-modal signal collection system incorporated a CMOS camera (60 Hz), NIR camera (50 Hz), microphone (44.1 kHz), and spectrometer (40 Hz). All synchronization is performed at the feature level rather than at the raw signal level. Prior to any temporal alignment, time-domain and frequency-domain features are independently extracted from each sensor's raw stream at its native sampling rate. Specifically, the melt pool images (60 Hz) and temperature field (50 Hz) each yield one feature vector per frame. For the acoustic signal (44.1 kHz), a sliding-window framing strategy is applied with a frame length of 1024 samples and a hop size of 512 samples, yielding a feature output rate of approximately 86 Hz (44100/512). The

Table 7
Mathematical definitions of features of acoustic signals.

Num.	Name	Formula	Description
1	Amplitude Envelope	$AE = \max(s_{(k)}[t{\cdot}K, (t+1){\cdot}K-1])$	Represents the envelope curve of the signal's amplitude variation over time, commonly used to describe the dynamic changes in amplitude of non-stationary signals.
2	Root Mean Square Energy	$RMS = \sqrt{\frac{1}{K}\sum_{k=t\cdot K}^{(t+1)\cdot K-1} s_{(k)}^2}$	Measures the average energy of the signal over a certain time window, reflecting the strength of the signal.
3	Zero Crossing Rate	$ZCR = \frac{1}{2}\cdot\sum_{k=t\cdot K}^{(t+1)\cdot K-1}\lvert\mathrm{sgn}(s_{(k)}) - \mathrm{sgn}(s_{(k+1)})\rvert$	An indicator of the number of times the amplitude changes from positive to negative in a signal, reflecting the content of high-frequency components in the signal.
4	Spectral Centroid	$SC = \left(\sum_{n=1}^{N} m_{t(n)}{\cdot}n\right)/\left(\sum_{n=1}^{N} m_{t(n)}\right)$	Weighted average of frequency values.
5	Spectral Bandwidth	$SBW = \left(\sum_{n=1}^{N}\lvert n - SC_t\rvert{\cdot}m_{t(n)}\right)/\left(\sum_{n=1}^{N} m_{t(n)}\right)$	Weighted average of frequency distance from SC (energy spread).
6	Spectral Roll-off	$SR = i$ is.t. $\sum_{n=1}^{i}\lvert m_{t(n)}\rvert = \eta\sum_{n=1}^{N}\lvert m_{t(n)}\rvert$	Central frequency of the total energy's specific ratio (85%).
7	Spectral Spread	$SS = \sqrt{\left(\sum_{n=1}^{N}(f_{(n)} - SC_t)^2{\cdot}m_{t(n)}\right)/\left(\sum_{n=1}^{N} m_{t(n)}\right)}$	Measures the dispersion of spectral energy around the spectral centroid.
8	Spectral Flatness	$SFt = \left(\prod_{n=1}^{N} m_{t(n)}\right)^{\frac{1}{n}}/\left(\frac{1}{n}\sum_{n=1}^{N} m_{t(n)}\right)$	Geometric mean divided by the arithmetic mean of the spectrum
9	Spectral Entropy	$SE = \left(-\sum_{n=1}^{N} m_t(n){\cdot}\log(m_t(n))\right)/\log(N)$	Measure of the peaks of the spectrum.
10	Spectral Flux	$SFx = \left(\sum_{n=1}^{N}\lvert m_{t(n)} - m_{t-1(n)}\rvert^p\right)^{\frac{1}{p}}$	Measure of the change of the spectrum over time.

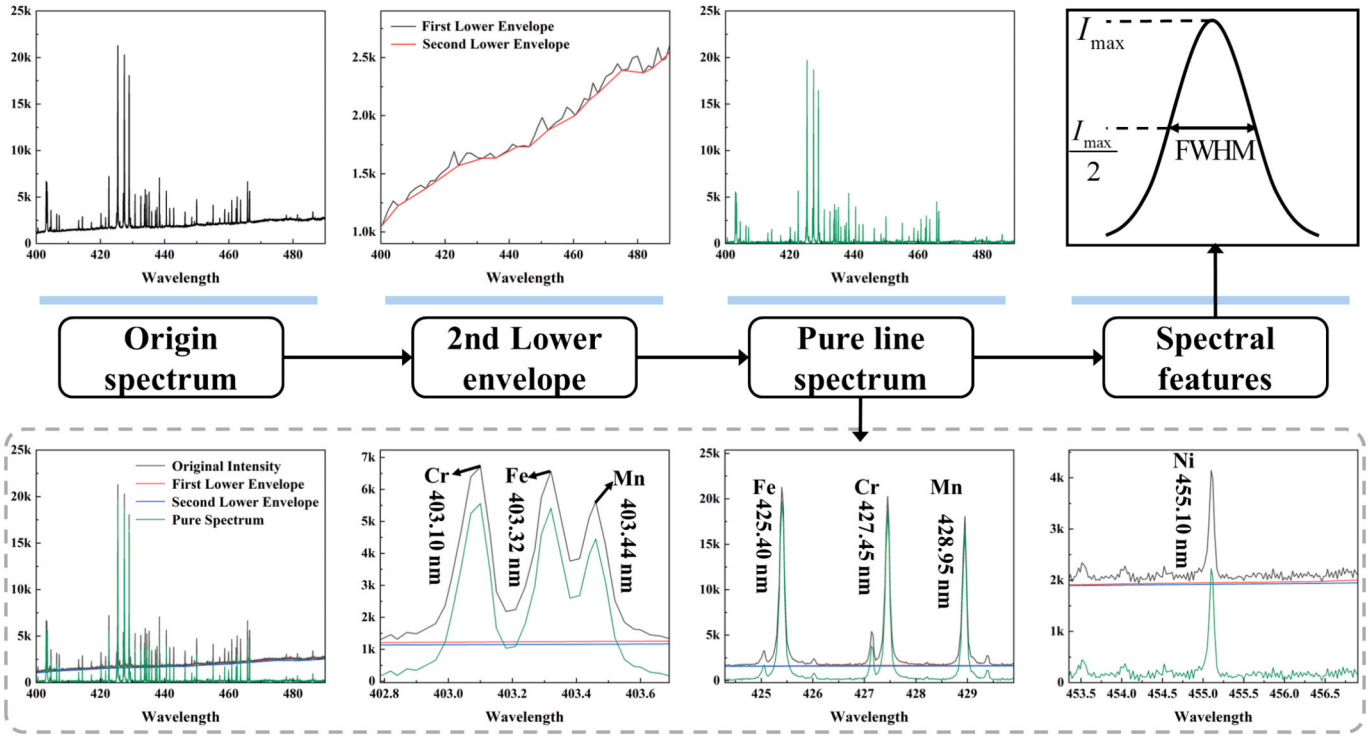

Fig. 9. Flowchart for spectral feature extraction.

spectrum (40 Hz) yields one feature vector per scan.

Initially, the common temporal range for all sensor data is determined through analysis of timestamps extracted from each sensor's features, with relative temporal offsets calculated accordingly. A unified timeline at 40 Hz was subsequently established as the synchronization benchmark. This frequency was selected to preserve information integrity for low-frequency sensors, matching the lowest-rate sensor (spectrometer) to prevent information loss from higher-rate modalities. The temporal alignment of sensor features was achieved using piecewise cubic Hermite interpolation (PCHIP), with linear interpolation employed for scenarios with insufficient data points to maintain numerical stability. Finally, synchronization quality was validated by assessing data coverage and temporal continuity of the interpolated features. Thus, multi-sensor data with varying sampling rates were unified onto a common temporal axis, resulting in a multi-dimensional feature matrix encompassing geometric features, temperature features, acoustic features, and spectrum features. This matrix provides a robust data foundation for subsequent multi-modal analysis and quality prediction in the laser deposition process, as illustrated in Fig. 10.

Prior to fusion analysis, individual correlation analysis was performed on the features of each sensor modality using Pearson correlation coefficients given in Equation (1). Feature selection follows a three-step criterion of "physical significance prioritization – redundancy elimination – process sensitivity quantification". Specifically, features with clear physical interpretations were retained first. Subsequently, highly redundant features were identified and removed by applying a correlation thresholds ($|r| > 0.9$). Finally, the remaining features were quantitatively assessed based on their sensitivity to process variations to

Table 8
Mathematical definitions of time-domain spectral features.

Num.	Parameter	Calculation Method
1	Background Average (BGA)	$\mathrm{BGA} = \frac{1}{N}\sum_{\lambda_i \in [400,495]} I_{\mathrm{bg}}(\lambda_i)$
2	Cr Peak Intensity	$\mathrm{CrP} = I_{\mathrm{peak}}(\lambda_{403.1\mathrm{nm}})$
3	Cr FWHM	$\mathrm{CrF} = \max(\Lambda) - \min(\Lambda)$ $\Lambda = \{\lambda \in [\lambda_a, \lambda_b] \mid I(\lambda_{403.1\mathrm{nm}}) \geq \frac{1}{2}\cdot \max_{\lambda \in [\lambda_a, \lambda_b]} I(\lambda)\}$
4	Fe Peak Intensity	$\mathrm{FP1} = I_{\mathrm{peak}}(\lambda_{403.32\mathrm{nm}})$
5	Fe FWHM	$\mathrm{FF1} = \max(\Lambda) - \min(\Lambda)$ $\Lambda = \{\lambda \in [\lambda_a, \lambda_b] \mid I(\lambda_{403.32\mathrm{nm}}) \geq \frac{1}{2}\cdot \max_{\lambda \in [\lambda_a, \lambda_b]} I(\lambda)\}$
6	Fe Peak Intensity	$\mathrm{FP2} = I_{\mathrm{peak}}(\lambda_{425.4\mathrm{nm}})$
7	Fe FWHM	$\mathrm{FF2} = \max(\Lambda) - \min(\Lambda)$ $\Lambda = \{\lambda \in [\lambda_a, \lambda_b] \mid I(\lambda_{425.4\mathrm{nm}}) \geq \frac{1}{2}\cdot \max_{\lambda \in [\lambda_a, \lambda_b]} I(\lambda)\}$
8	Mn Peak Intensity	$\mathrm{MnP} = I_{\mathrm{peak}}(\lambda_{403.4\mathrm{nm}})$
9	Mn FWHM	$\mathrm{MnF} = \max(\Lambda) - \min(\Lambda)$ $\Lambda = \{\lambda \in [\lambda_a, \lambda_b] \mid I(\lambda_{403.4\mathrm{nm}}) \geq \frac{1}{2}\cdot \max_{\lambda \in [\lambda_a, \lambda_b]} I(\lambda)\}$
10	Ni Peak Intensity	$\mathrm{NiP} = I_{\mathrm{peak}}(\lambda_{455.1\mathrm{nm}})$
11	Ni FWHM	$\mathrm{NiF} = \max(\Lambda) - \min(\Lambda)$ $\Lambda = \{\lambda \in [\lambda_a, \lambda_b] \mid I(\lambda_{455.1\mathrm{nm}}) \geq \frac{1}{2}\cdot \max_{\lambda \in [\lambda_a, \lambda_b]} I(\lambda)\}$

select the key features from each modality. Following this, fused correlation analysis was conducted on the key features from the four sensing signals. The resulting correlation matrix was visualized as a heatmap, where color intensity and ellipse orientation represent the strength and direction of the correlations between cross-modal features, respectively. This analytical approach enables identification of feature coupling relationships among different sensor modalities, providing a foundation for multi-modal feature fusion and dimensionality reduction.

$$r_{xy} = \sum_{i=1}^{n}(x_i - \overline{x})(y_i - \overline{y}) \Big/ \left(\sqrt{\sum_{i=1}^{n}(x_i - \overline{x})^2}\sqrt{\sum_{i=1}^{n}(y_i - \overline{y})^2}\right) \quad (1)$$

4. Results and discussion

During the manufacturing process, multi-source signals closely associated with the melt pool are intrinsically coupled, containing profound insights into the metal powder melting mechanism. Quantitative correlation analysis can effectively elucidate the synergistic or complementary relationships among signals by calculating correlation coefficients between feature values.

4.1. Spatiotemporal feature fusion of multi-source sensing signals

The acquired thermal images, melt pool images, acoustic signals, and plasma spectral signals were first aligned along a unified timeline, as illustrated in Fig. 11(a). Time-domain features were then extracted and fused from these synchronized multi-source signals. The extracted features included ten descriptors of melt pool geometry from melt pool images, eight descriptors of thermal characteristics from thermal images, ten descriptors of reaction intensity from acoustic signals, and eleven descriptors of elemental excitation states from plasma spectra. Correlation analysis was subsequently performed on the features within each signal type to enable feature-level fusion.

As shown in Fig. 11(b), calculating the Pearson correlation coefficients among visible image features revealed a strong positive correlation between the melt pool area (VA) and both the major axis (VMa, $r = 0.98$) and minor axis (VMi, $r = 0.97$), indicating that the area closely corresponds to the geometric axial dimensions of the melt pool contour. A correlation of 0.93 was also observed between the area and entropy (VEt), suggesting that larger areas encompass more complex textural information. A strong negative linear correlation (Pearson coefficient of −0.92) was found between the area and homogeneity (VH). These results demonstrate that the area and entropy effectively assess variations in melt pool geometry and textural complexity. However, the perimeter (VP), circularity (VCc), and contrast (VCt) showed no significant correlation with other time-domain features, indicating their potential role as complementary signals for observing geometric and textural variations.

Fig. 11(c) shows that among the near-infrared image features, only the thermal area (TA) and thermal perimeter (TP) were strongly correlated (Pearson coefficient = 0.97), while other time-domain features exhibited negligible correlations. For the acoustic signal features (Fig. 11(d)), some pairs, such as root mean square energy (RMS) with spectral flux (SFx), spectral roll-off (SR) with spectral centroid (SC), spectral spread (SS) with spectral bandwidth (SBW), spectral entropy (SE) with RMS and SFx), showed correlations, whereas others were weakly associated (Pearson values less than 85%). Consequently, relying

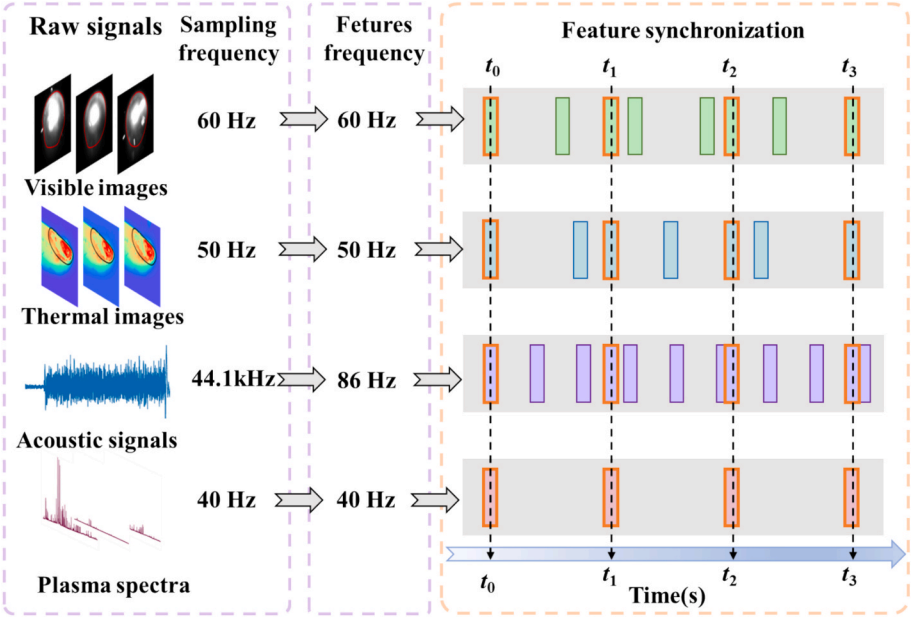

Fig. 10. Synchronization strategy.

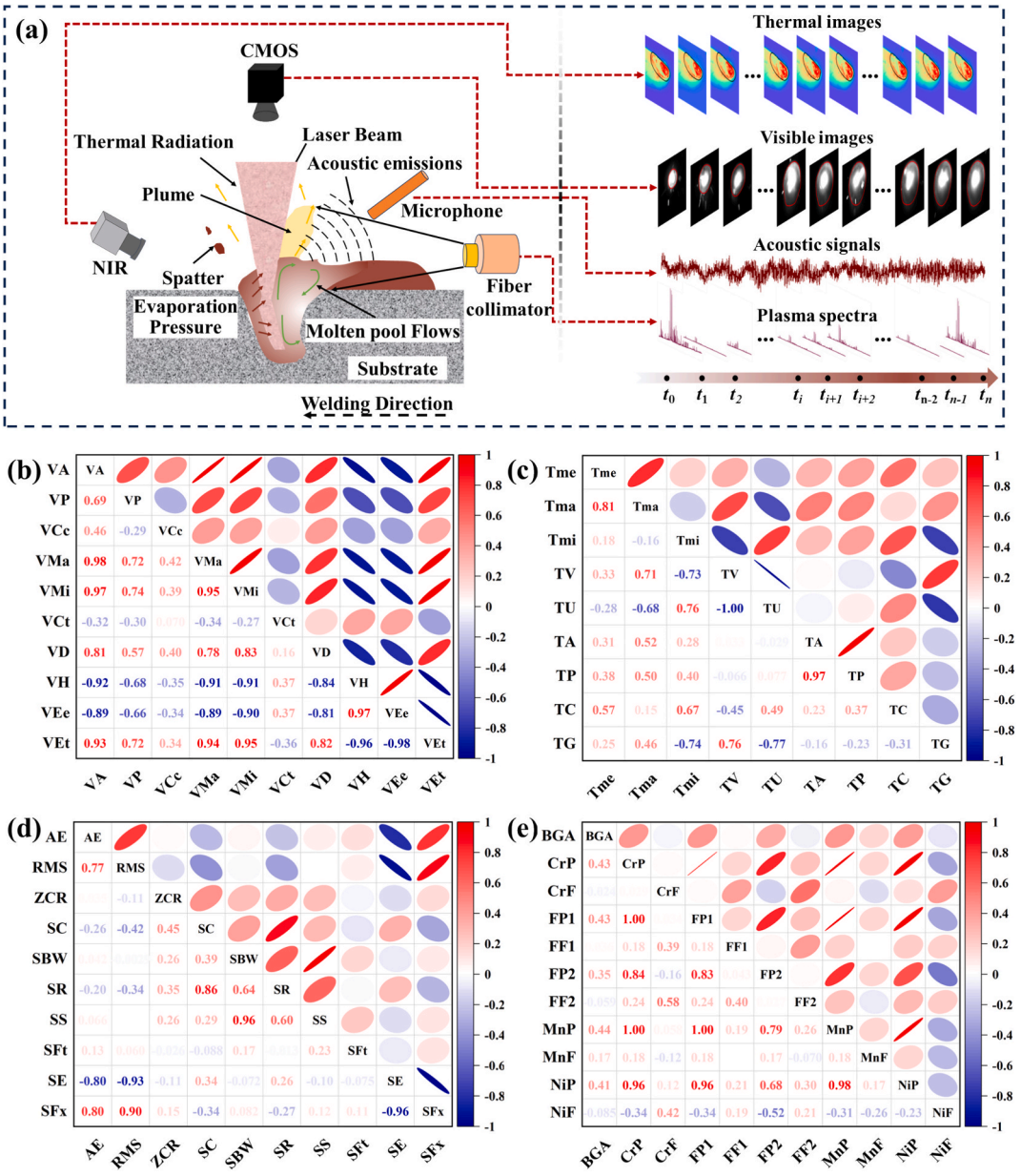

Fig. 11. Spatiotemporal feature fusion of multi-source sensing signals: (a) Acquired thermal images, melt pool images, acoustic signals, and plasma spectral signals; (b)Pearson coefficients of geometric morphology features; (c) Pearson coefficients of temperature field features; (d) Pearson coefficients of acoustic signal features; (e) Pearson coefficients of plasma spectral features.

solely on data-driven correlation analysis is insufficient for extracting key features from infrared and acoustic signals for process evaluation. Therefore, based on the physical laws of the melt pool deposition process and empirical data [29], Tma, TV, TA, and TG were preliminarily selected as indicators for temperature variation, while AE, ZCR, SC, SBW, SFt, and SFx were chosen to represent reaction intensity.

As shown in the supporting file, separating the background from the spectral signals identified 80 elemental line spectra, indicating the presence of multiple metal elements in the printed material. Cross-referencing with the NIST database assigned 29 lines to Cr, 41 to Fe, 80 to Mn, and 20 to Ni. This study selected the line spectral peak intensities and full width at half maximum (FWHM) corresponding to four elements Cr, Fe, Ni, and Mn at specific wavelengths (Cr (λ=403.1 nm), Fe (λ=403.32 nm and 425.4 nm), Ni (λ=403.44 nm), and Mn (λ=455.1 nm)) as well as the background spectral mean for correlation analysis.

Fig. 11(e) shows that the background spectral mean (BGA) did not correlate significantly with the peak intensities (CrP, FP1, FP2, MnP, NiP) and their corresponding line spectral FWHM (CrF, FF1, FF2, MnF, NiF) of the elements. The Fe peak at λ = 425.4 nm (FP2) showed weak correlation with the peaks of the other three elements, while the Cr peak (CrP, λ = 403.1 nm) correlated noticeably with the Fe (λ = 403.32 nm), Mn (MnP, λ = 455.1 nm), and Ni (NiP, λ = 403.44 nm) peaks. Due to the low content of elements other than Fe and Cr, their spectral lines are susceptible to background interference, making accurate feature extraction challenging. Thus, the time-domain features of Fe and Cr, namely CrP, CrF, FP2, FF2 of Fe and Cr, were selected as the core indicators for subsequent analysis. Table 9 presents the initially extracted time-domain features of visual images, infrared images, acoustic signals, and plasma spectra.

Pearson coefficients among the selected time-domain feature values were further calculated to assess the interaction patterns among different signal features. As shown in Fig. 12, the features from the four sensing signals exhibit complementary relationships. This finding indicates that the integrated use of these multi-source features facilitates a

Table 9
Results of feature selection for multi-source signals.

Feature	Name	Abbreviation
Geometric features	Area	VA
	Perimeter	VP
	Circularity	VCc
	Contrast	VCt
	Entropy	VEt
Temperature features	Max Temperature	Tma
	Temperature Variance	TV
	Max Gradient	TG
	Area	TA
Acoustic features	Amplitude Envelope	AE
	Zero Crossing Rate	ZCR
	Spectral Centroid	SC
	Spectral_Bandwidth	SBW
	Spectral_Flatness	SFt
	Spectral Flux	SFx
Spectrum features	Background Average	BGA
	Cr_403.10 Peak Intensity	CrP
	Cr_403.10 FWHM	CrF
	Fe_425.40 Peak Intensity	FP2
	Fe_425.40 FWHM	FF2

comprehensive evaluation and monitoring of melt pool variations during the printing process.

4.2. *Correlation between process parameters and multi-source signal features*

Fusion analysis at the data level of the time-domain features from multi-source signals reveals that correlation coefficient calculations can effectively clarify the interrelationships for most signals, thereby enabling the extraction of key signal features. However, for acoustic signals and thermal images, this data-centric approach proves inadequate for elucidating the underlying coupling mechanisms and fails to reliably identify signal values suitable for process monitoring. It was found that variations in multi-source signal feature values are often closely linked to process parameters.

As shown in Fig. 13, geometric features, temperature features, reaction intensity, and material element excitation state of the melt pool are extracted and analyzed from captured visible light images, thermal images, acoustic signals, and plasma spectra. The influence of process parameters on time-domain features is analyzed by controlling single process parameter variations. Most time-domain feature values from multi-source signals increase with increasing laser power (Fig. 13(a1, a2, a5, b1, b2, b4, c1,c6, d1, d4)). This consistent trend indicates that the interactions among multi-source signal features can be explored from a process-oriented perspective, allowing for the establishment of quantitative links between the process phenomena and the monitored signals. Such quantitative relationships are crucial for accurately extracting salient signal features and precisely evaluating process status.

For certain other signal features, such as image contrast (Fig. 13(a3)) and spectral bandwidth (Fig. 13(c4)), their relationship with process

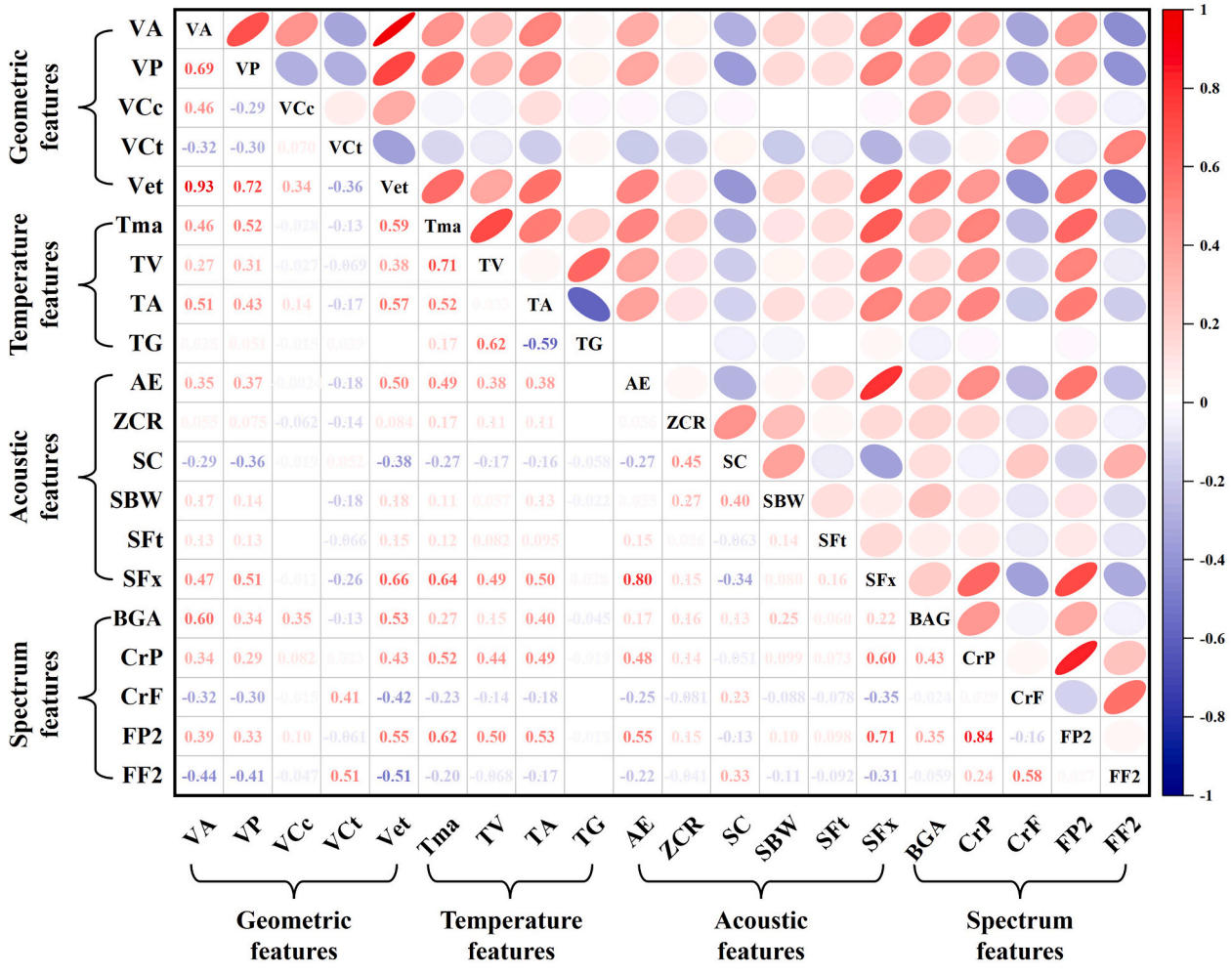

Fig. 12. Fusion analysis of key multi-source heterogeneous signal feature values based on correlation calculation.

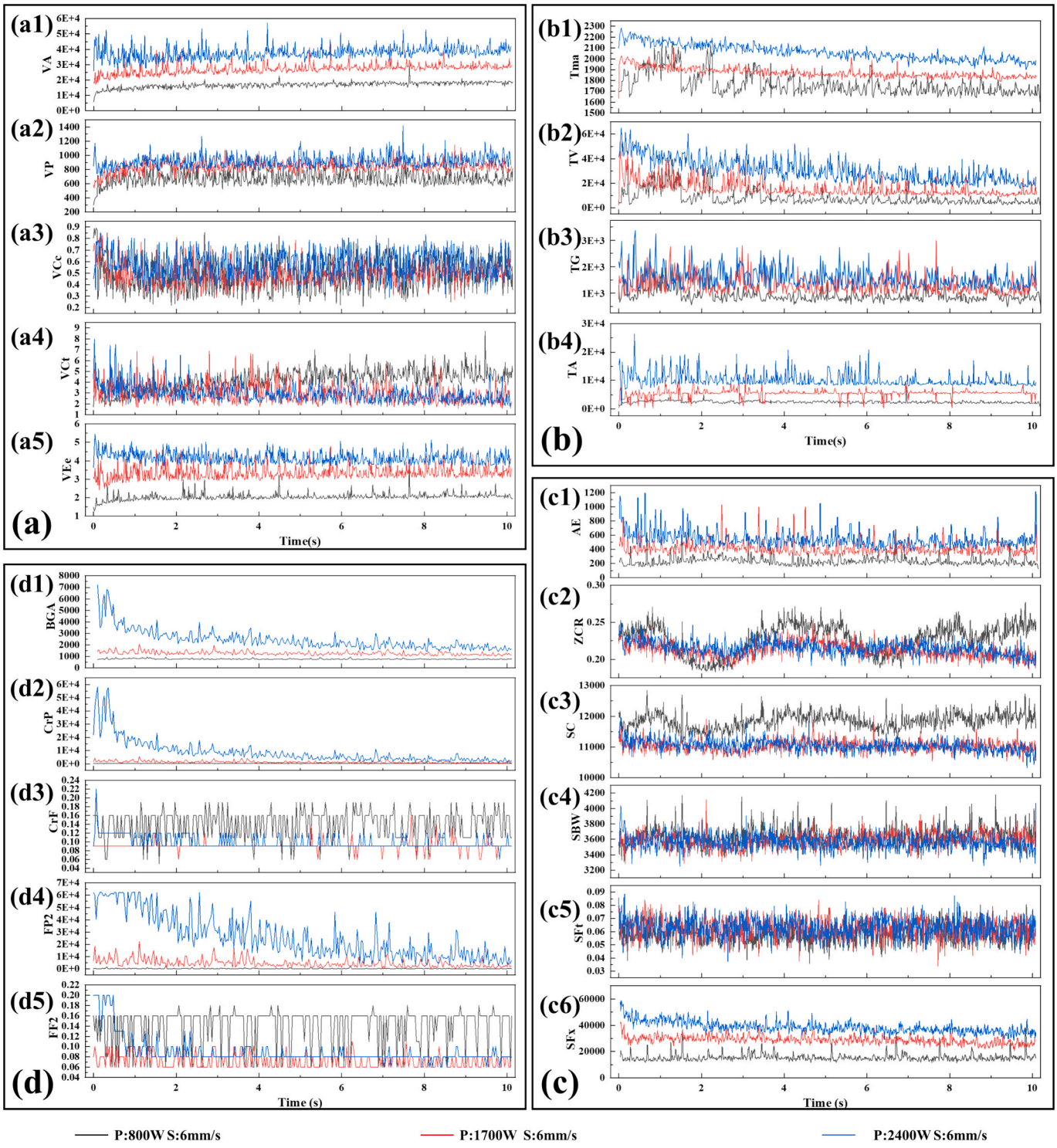

Fig. 13. Time-domain distribution of melt pool geometric feature values: (a) Geometric morphology features:(a1) VA, (a2) VP, (a3) VCc, (a4) VCt, (a5)VEt; (b) Temperature field features:(b1) Tma, (b2) TV, (b3)TG, (b4)TA; (c) Acoustic signal features:(c1)AE, (c2)ZCR, (c3)SC, (c4)SBW, (c5)SFt, (c6)SFx; (d) Plasma spectral features: (d1)BGA, (d2)CrP, (d3)CrF, (d4)FP2, (d5)FF2.

parameters cannot be readily deduced through qualitative observation of their temporal evolution. Consequently, we further computed the global average of these time-domain feature values along the entire single-track path under different process parameter combinations. This approach provides a comprehensive basis for uncovering the quantitative correlation relationships between process parameters and melt pool features.

4.2.1. *Melt pool geometric features*

Fig. 14(a) illustrates that at a constant scanning speed, the melt pool area increases as the laser power rises from 600 W to 2600 W in 100 W increments. This trend occurs because higher energy input melts more powder particles, thereby expanding the melt pool size. Conversely, the melt pool area decreases with increasing scanning speed, resulting from the reduced energy input per unit time, which leads to insufficient powder melting. As shown in Fig. 14(b), melt pool perimeter increases

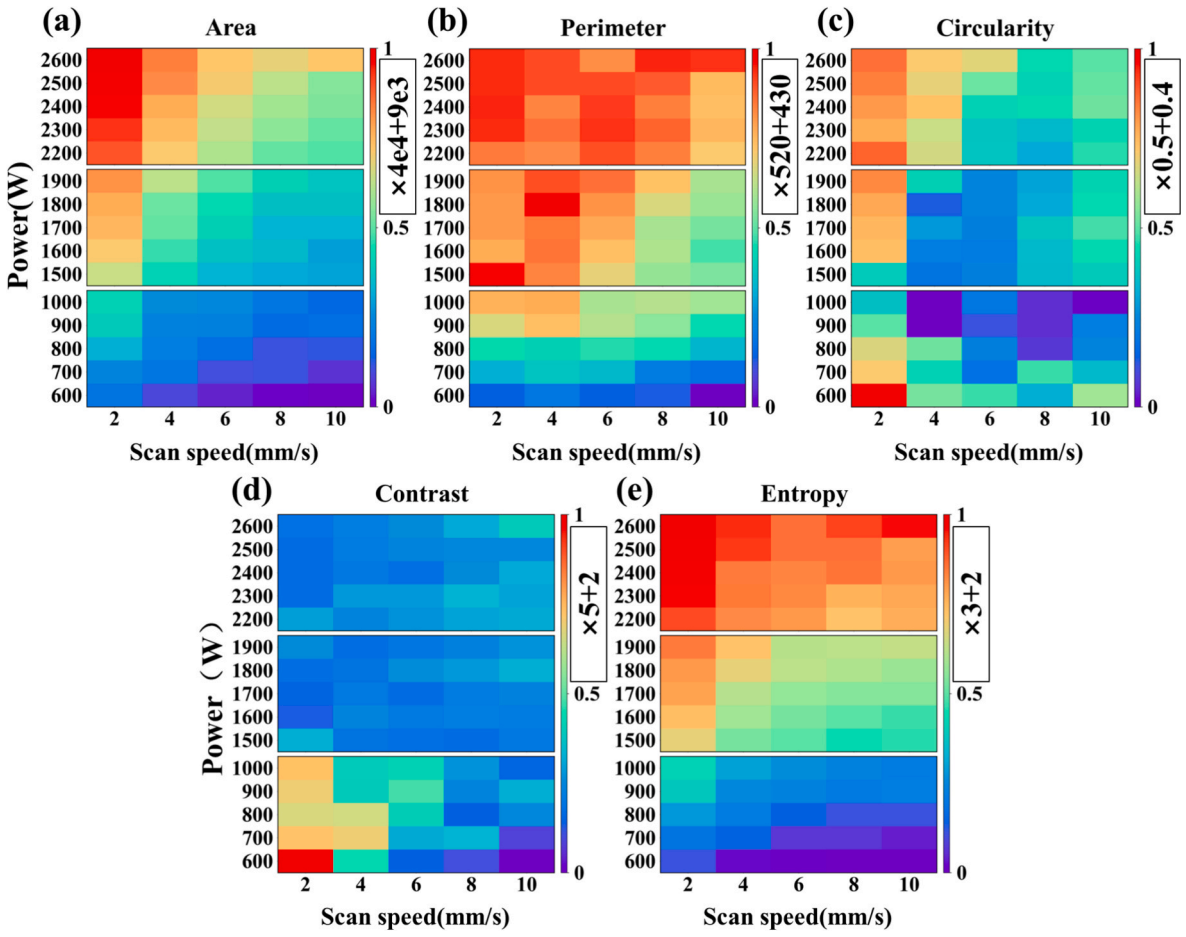

Fig. 14. Spatial fusion analysis of visible light feature values under different parameters: (a) Area; (b) Perimeter; (c) Circularity; (d) Contrast; (e)Entropy.

with laser power and decreases with scan speed. However, at specific powers (e.g., 1500 W and 1800 W) and within the high power range (2200 W-2600 W), the relationship between perimeter and scanning speed becomes nonlinear, indicating melt pool shape instability with an irregular, serrated contour pattern.

Fig. 14(c) shows the variation in melt pool circularity with process parameters. At a scanning speed of 2 mm/s, circularity gradually decreases as power increases from 600 W to 1000 W. This indicates that although energy input increases, insufficient convection hinders melt pool stabilization. When laser power ranges from 1500 W to 1900 W, circularity increases with power, indicating that the melt pool becomes fully molten and forms a nearly circular morphology due to adequate energy input. At higher power levels (2200–2600 W), circularity remains relatively unchanged, as excessive energy input increases melt depth and weakens the melt pool's tendency to expand uniformly in all directions. At scanning speeds of 4 mm/s and 6 mm/s, circularity first decreases and then increases with increasing laser power. Notably, at higher speeds of 8 mm/s and 10 mm/s, circularity shows negligible sensitivity to power variations. This phenomenon reflects the existence of a specific process window for scanning speed (approximately 4–6 mm/s). Outside this window, the system is either in a thermally saturated (low speed) or thermally deficient (high speed) state, where power adjustments cannot effectively regulate melt pool circulation.

As shown in Fig. 14(d), the melt pool contrast shows no clear correlation with process parameters in the medium- and high-power ranges. However, in the low-power range, contrast gradually decreases with increasing scanning speed, indicating significant melt pool surface fluctuations under these conditions. Furthermore, the melt pool entropy increases gradually with laser power and decreases with scanning speed (Fig. 14(e)). This suggests that as energy input per unit time increases, the melt pool transitions progressively from a stable conduction mode to a transition mode, and finally to a complex keyhole mode. Thus, the geometric features extracted from melt pool images effectively characterize the evolution patterns of the melt pool.

4.2.2. *Melt pool temperature*

As shown in Fig. 15, NIR camera was employed to acquire in-situ thermal images of the melt pool. Combined with threshold extraction and edge detection techniques, the influence of process parameters on the melt pool temperature was characterized in-situ. Fig. 15(a) shows the effect of laser power and scanning speed on the maximum melt pool temperature. At a fixed scanning speed, the maximum temperature gradually increases with laser power, which is attributed to the increased energy input into the melt pool per unit time. Furthermore, as the scanning speed increases from 2 mm/s to 10 mm/s, the instantaneous maximum temperature decreases at low power levels (600 W and 700 W). In contrast, at power levels above 700 W, the maximum temperature either shows no significant change or increases with scanning speed. At low power, increased speed leads to insufficient energy density and temperature decrease. At higher power with adequate energy density, the increased speed causes the elongation of the comet-shaped melt pool tail and a redistribution of heat, maintaining or even increasing the instantaneous temperature stability in local regions.

As shown in Fig. 15(b), the temperature variance values increase with laser power, likely due to localized overheating caused by high energy input alongside insufficient heating in other areas, leading to enhanced temperature fluctuations. The temperature variance also mostly increases with scanning speed. Notably, at 600 W and 700 W, the

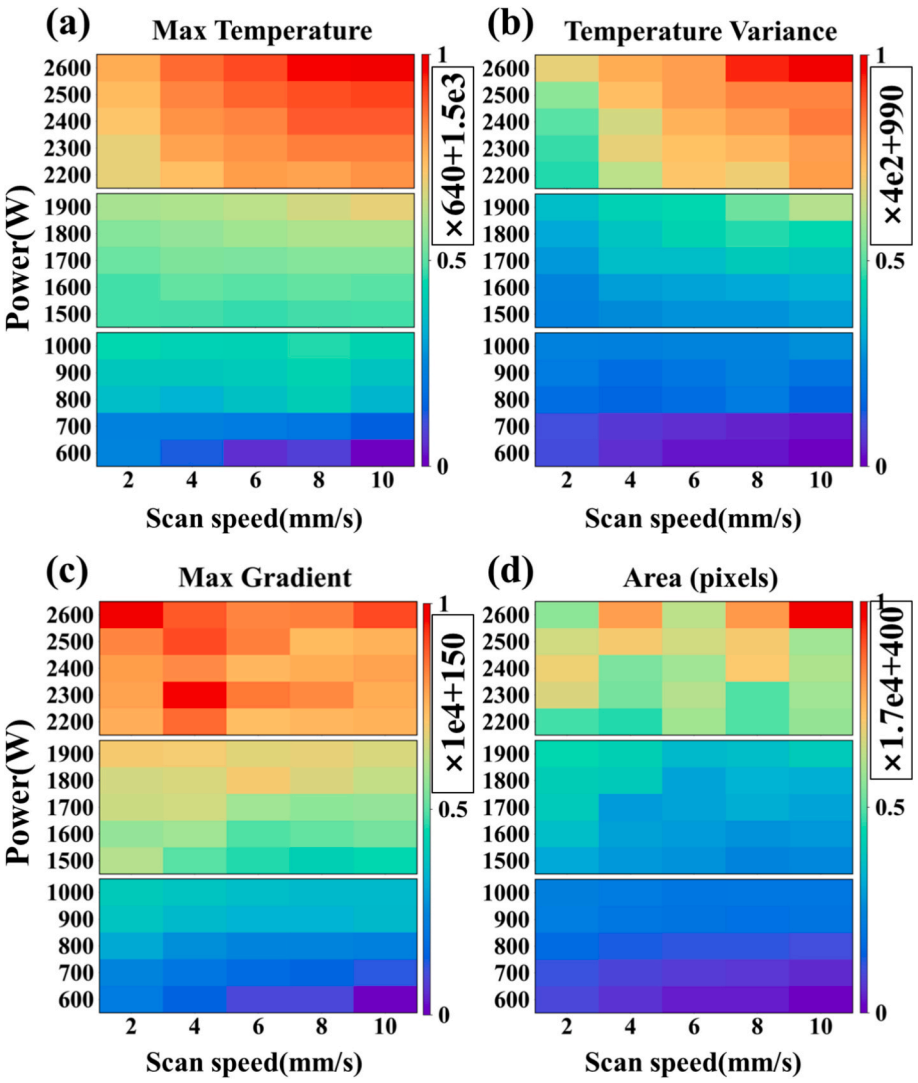

Fig. 15. Spatial fusion analysis of temperature feature values under different parameters: (a) Max temperature; (b) Temperature variance; (c) Max gradient; (d) Area.

melt pool temperature fluctuations remain moderate because the low energy input results in a relatively small temperature gradient within the melt pool (Fig. 15(c)).

As shown in Fig. 15(d), the high-temperature zone area expands with increasing laser power at a constant scanning speed. This is because higher energy input causes the material to absorb more heat, forming a larger molten zone. When the power is fixed within the 600 ~ 1000 W, the high-temperature area shows no significant change with scanning speed. When power is fixed in 1500 ~ 1900 W, the area slightly expands with increasing scan speed. However, at ultra-high power levels (2200 ~ 2600 W), the high-temperature area exhibits random variations. This phenomenon is caused by keyhole instability and plasma formation triggered by ultra-high power, as shown in Fig. 17(b) and (e), where fluctuations in vapor recoil pressure cause the melt pool state to switch randomly between different modes, resulting in stochastic changes in the thermal area.

4.2.3. Melt pool reaction intensity

Acoustic signals generated by laser-material interaction can reveal melt pool reaction intensity [10]. As shown in Fig. 16, a microphone was used to capture acoustic signals during deposition. Melt pool reaction intensity during deposition was elucidated by extracting time-domain and frequency-domain features of the original signal and analyzing their evolution with process parameters.

Fig. 16(a) indicates that at a fixed scanning speed, the melt pool reaction intensity increases with laser power. This is attributed to the higher power enabling the laser beam to penetrate deeper material layers, thereby increasing the melt pool depth. Simultaneously, the wider energy distribution results in a corresponding increase in melt pool width, allowing more material in the melting process and further enhancing reaction intensity. At a constant laser power, the reaction intensity also increases with scanning speed. This suggests that although the higher scanning speed reduces the laser dwell time per unit area under constant total energy input, it leads to a decrease in both melt pool depth and width, reducing the melt pool volume. A smaller melt pools facilitates heat exchange with the surrounding environment, increasing the cooling rate and consequently intensifying reaction rates within the melt pool.

The spectral characteristics of the acoustic signal were characterized using the Zero-crossing rate and spectral centroid. As shown in Fig. 16 (b) and (c), the zero-crossing rate and spectral centroid values in the low power range are mostly higher than those in medium and high power ranges. However, at a scanning speed of 10 mm/s, both zero-crossing rate and spectral centroid initially increase and then decrease with increasing power. This signal reversal phenomenon reflects a transition of melt pool physical processes from low-frequency dominance (insufficient melting [30]) to high-frequency dominance (surface tension oscillation[10,31]), and back to low-frequency dominance (Marangoni

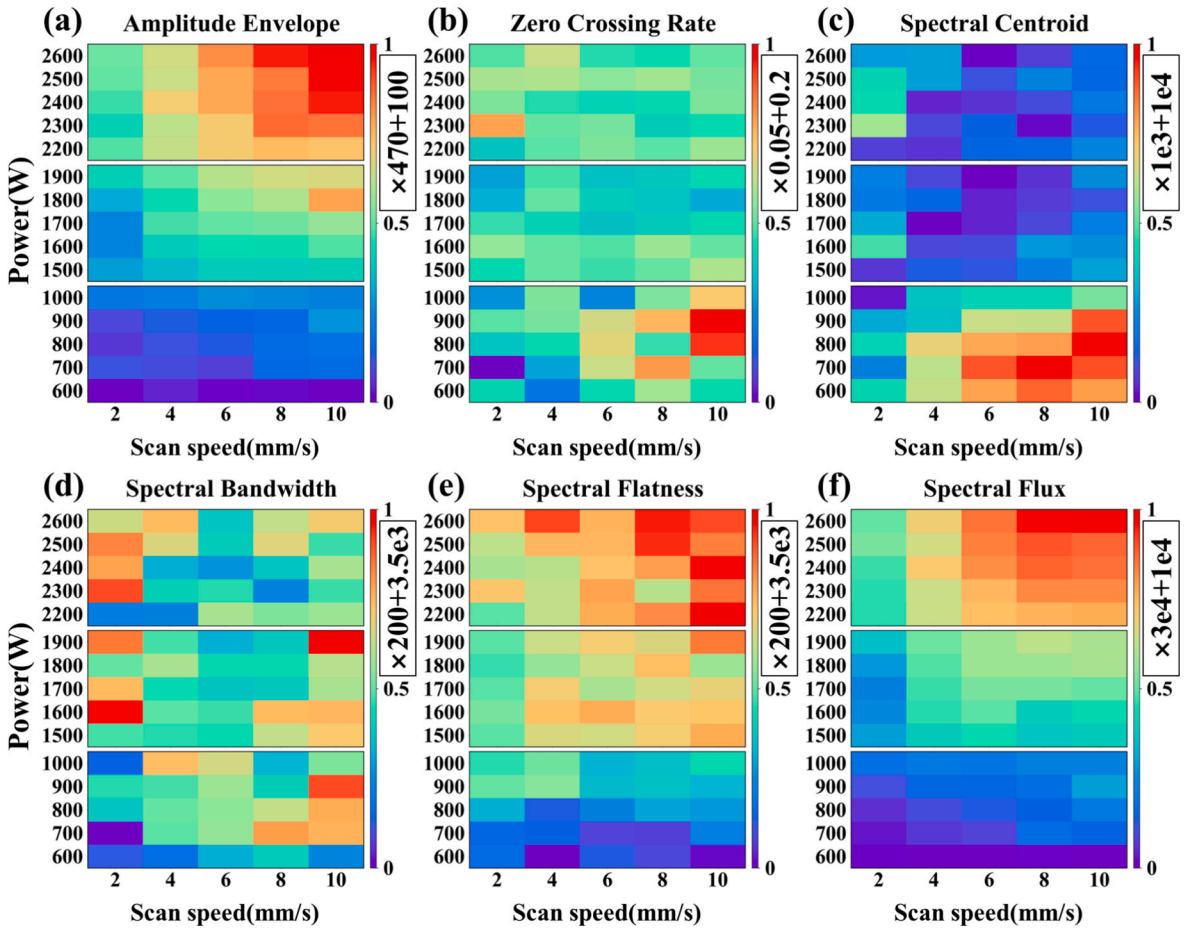

Fig. 16. Spatial fusion analysis of acoustic signal feature values under different parameters: (a) Amplitude envelop; (b) Zero crossing Rate; (c) Spectral centroid; (d) Spectral bandwidth; (e) Spectral flatness; (f) Spectral flux.

convection, pore oscillation[32,33]).

Analysis of the spectral bandwidth of the acoustic signal reveals no clear correlation with variations in process parameters, as shown in Fig. 16(d). This verifies the nonlinearity of spectral bandwidth response to process parameters, and its inadequacy for monitoring and analyzing melt pool evolution patterns. In contrast, both the spectral flatness and spectral flux of acoustic signals increase with increasing power, as shown in Fig. 16 (e) and (f). Notably, spectral flux exhibits an approximately positive linear relationship with power variation. This is because high power drives the melt pool into a violent boiling, exciting evaporation, turbulence, and splashing. This generates broadband random noise that increases Spectral Flatness, while rapid spectral fluctuations elevate Spectral Flux.

4.2.4. *Material element excitation state*

During deposition, molten metal atoms are excited to different energy levels through high-temperature evaporation and transport. The intensity and distribution of plasma emission spectra directly reflect metal element concentration, plasma temperature, and electron density [34,35]. Real-time acquisition of plasma spectra during deposition and extraction of key spectral features enable the quantitative elucidation of the influence of process parameters on the excitation states of metal elements.

As shown in Fig. 17(a), the average background intensity of the plasma spectra is highest at a scanning speed of 2 mm/s. Across the three power ranges, the average background intensity initially increases and then decreases with increasing power. Within the scanning speed range of 4 mm/s to 10 mm/s, the variation in the average background intensity is not significant. Fig. 17 (b) and (d) show that under fixed scanning speeds, the plasma spectral peak intensities of Cr and Fe elements generally exhibit an upward fluctuation trend with increasing laser power. At fixed laser power levels, the peak intensities of most Cr and Fe elements also fluctuate with increasing scanning speed. Notably, under the parameter combinations of laser power at 700 W, 800 W, and 900 W with a scanning speed of 2 mm/s, the Cr spectral lines exhibit abnormally high peak intensities. This is primarily attributed to the significantly elevated average background intensity in this parameter range (Fig. 17(a)), coupled with the inherently weak line peaks generated by low-power excitation, leading to errors in feature peak value and FWHM extraction.

As shown in Fig. 17(b), within the low-power range, the FWHM values of the Cr element decrease with increasing power and scanning speed. However, at laser powers of 700 W, 800 W, and 900 W combined with a scanning speed of 2 mm/s, the Cr FWHM values are also affected by the high background, presenting abnormally high values. In the medium and high-power ranges, the FWHM variations are less pronounced. This phenomenon occurs because the spectral line FWHM is jointly determined by Doppler broadening (proportional to square root of temperature) and Stark broadening (dependent on electron density) [36–39]. At low power, competition between these two broadening mechanisms causes the FWHM to decrease with increasing power, whereas at high power levels, Stark broadening dominates, leading to FWHM stabilization [40,41]. This mechanism also explains the reduction in spectral line broadening observed with increasing scanning speed under low-power conditions.

Regarding the variation pattern of Fe element line FWHM values (Fig. 17(e)), distinct zonal characteristics can be observed under different scanning speeds. At scanning speeds of 2, 4, and 6 mm/s, the

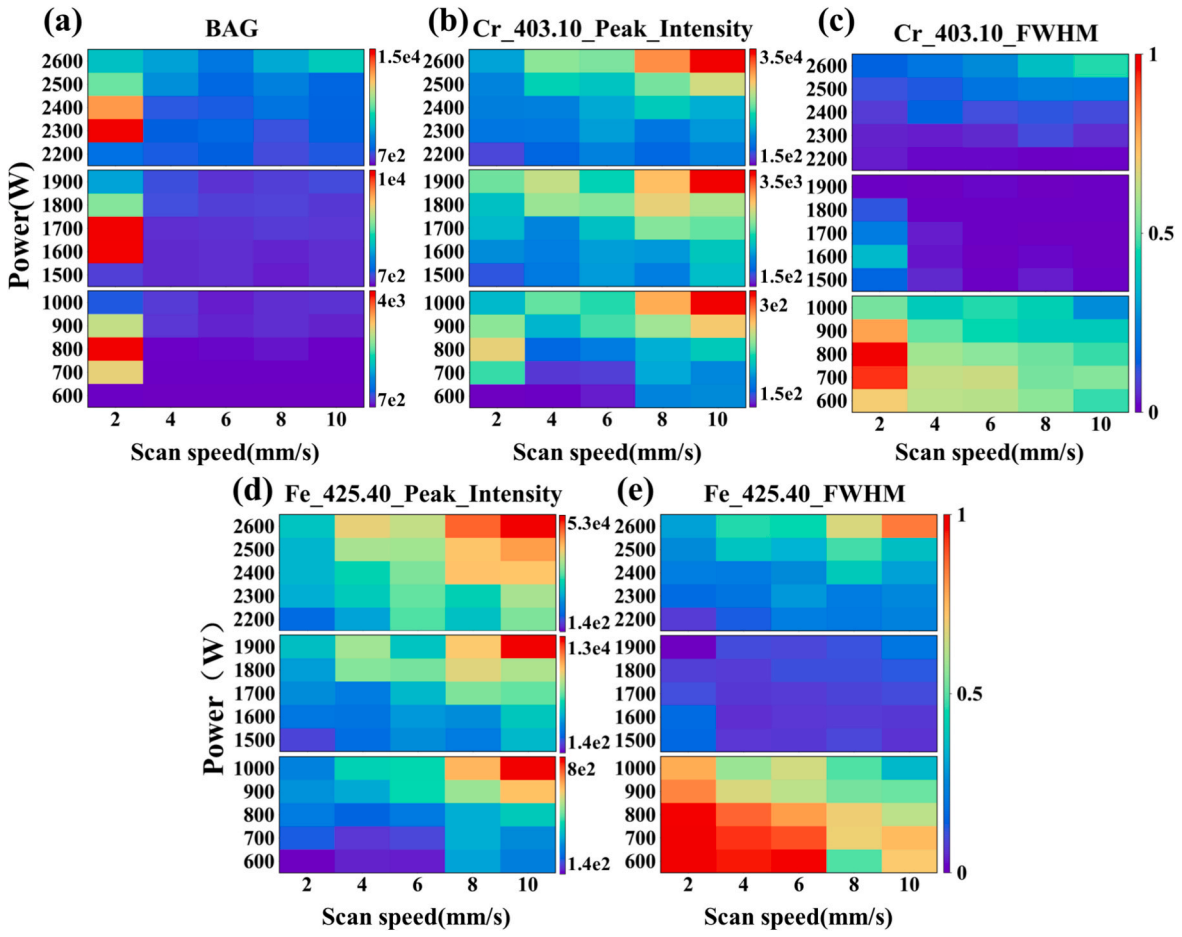

Fig. 17. Spatial fusion analysis of plasma emission spectral feature values under different parameters: (a) Background Average; (b) Cr Peak Intensity; (c) Cr FWHM; (d) Fe Peak Intensity; (e) Fe FWHM.

FWHM values gradually decrease as laser power increases from 600 W to 1000 W (low-power zone). As power continues to increase to 2600 W, the FWHM drops sharply to a lower level in the medium-power zone but shows a slight increasing trend in the high-power zone (2400–2600 W). When the scanning speed increases to 8 mm/s and 10 mm/s, the FWHM in the low-power zone first increases and then decreases, remains low and relatively constant in the medium-power zone, and also recovers slightly in the high-power zone. From the perspective of scanning speed influence, at low power, FWHM generally shows a decreasing trend with increasing scanning speed, but exhibits abnormal fluctuations under specific parameter combinations (e.g., 600 W, 2 mm/s), possibly due to melt pool instability or plasma density fluctuations. At medium power levels, FWHM values are significantly lower and remain almost constant. At high power levels, FWHM gradually increases with scanning speed, with the most pronounced change at 2600 W. This trend is largely consistent with that of Cr FWHM, indicating that when the melt pool reaches its highest temperature at high power, the intensified electron collision frequency and energy transfer processes (Fig. 16(a, e, f)) enhance the Stark broadening effect, consequently causing the FWHM value to recover.

The time–frequency features of multi-source signals were extracted and analyzed across different process parameters. This process enabled the identification of key signals characterizing melt pool dynamics. Furthermore, it revealed quantitative correlations between these signal features and the melt pool geometric morphology, temperature features, reaction intensity, and plasma excitation state.

4.3. Quantitative relationships among process parameters, multi-source signals, and forming quality

The in-situ monitoring of melt pool dynamic behavior was achieved through the online acquisition and extraction of key signals. However, establishing reliable feedback control strategies based on these monitoring signals is ultimately critical for ensuring part quality. The L-DED process window can be effectively defined by analyzing the influence patterns of process parameters on geometric morphology. Integrating this window with the quantitative correlations between process parameters and multi-source signal features allows for the determination of appropriate signal value ranges, thereby providing precise quantitative guidance for process feedback and correction.

The width and height values of single-wall deposits under different process parameters were extracted to further analyze connections between multi-source signal features and geometric morphology. Fig. 18 (a) shows the macroscopic geometrical morphology of single beads fabricated at a fixed power of 1700 W with varying scanning speeds. It can be observed that the average bead width decreases with increasing scan speed (Fig. 18(b)). The deposit surface appears smooth at scanning speeds of 2 mm/s, 4 mm/s, and 6 mm/s. However, pronounced surface ripples emerge when the scanning speed increases to 8 mm/s and 10 mm/s, as indicated by the white boxes in Fig. 18(a).

The width and height values along the bead length direction were extracted by acquiring the point cloud data of the single beads (Fig. 18 (b)). At scanning speeds of 2 mm/s and 4 mm/s, the width values fluctuate within a range of 2.8 mm to 3.0 mm, with no significant variation. In contrast, at scanning speeds of 6 mm/s, 8 mm/s, and 10

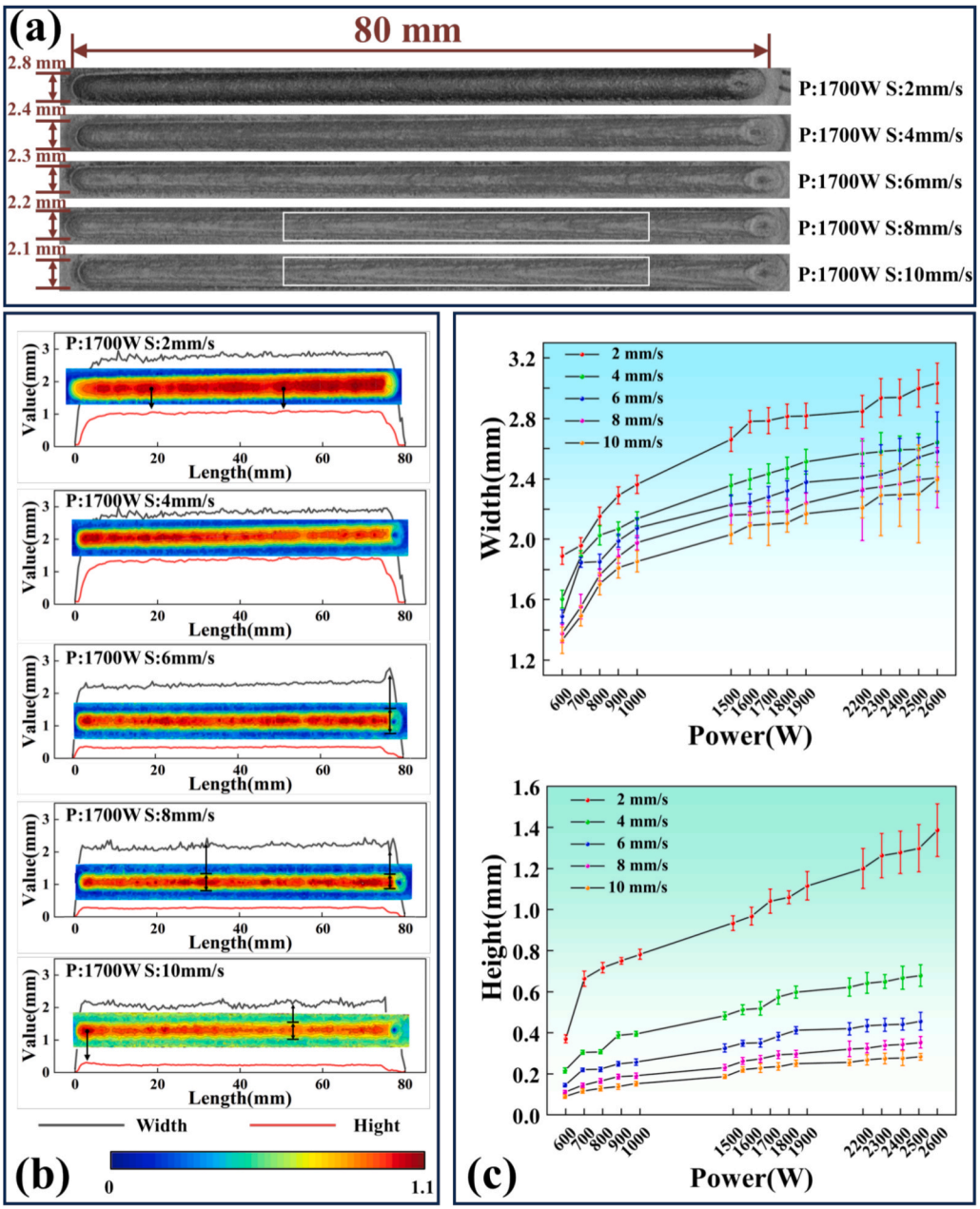

Fig. 18. Statistical plots of forming width and height: (a) Macroscopic morphology; (b) Forming width and height variations (1700 W); (c) Width and height variations under different parameters.

mm/s, the width values fluctuate between 2.0 mm and 2.5 mm, with the fluctuation amplitude at the end of the bead reaching up to 0.5 mm.

Fig. 18(c) presents statistical plots of the width and height values under different process parameters. It is evident that, at a fixed scanning speed, both the formed width and height increase with laser power. Specifically, the increase is more rapid at low power levels and becomes relatively gradual at medium and high power levels. Under constant laser power, both width and height decrease with increasing scanning speed. These findings underscore the importance of appropriate process window settings for guaranteeing the geometric dimensional accuracy of formed deposits.

The width and height data from the middle stable region (4–76 mm) of each single bead were extracted to define the laser power and scan speed window for L-DED. The coefficient of variation and normalized gradient magnitude of these data were calculated according to Equations (2) and (3) to characterize the geometrical consistency and surface continuity of the single beads, respectively. Through normalization, both metrics were mapped to the [1] interval, constructing a forming quality scoring function. A score closer to 1 indicates superior forming quality and higher geometrical accuracy, whereas a score approaching 0 signifies poor forming quality.

$$CV = \frac{\delta}{\mu} \tag{2}$$

where δ is the standard deviation and μ is the mean.

$$S = \frac{\mathrm{std}(\nabla x)}{\mathrm{mean}(x)} \tag{3}$$

where $\nabla x = x_{i+1} - x_i$ is the first-order difference.

Fig. 19 presents the quality scoring results under various process parameters. It is clearly observed that high single-bead forming quality is achieved within specific combinations of scanning speed and laser

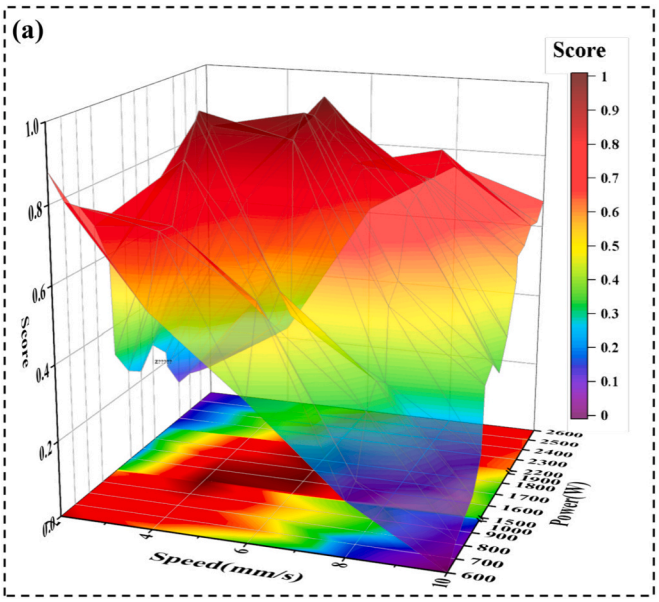

Fig. 19. Forming scores under different parameters evaluated based on width and height variations.

power (red regions in the figure). Accordingly, these parameter ranges are defined as the stable process window for L-DED. Specifically, the optimal scanning speed ranges from 2 to 6 mm/s at a laser power of 600–1000 W. The optimal scanning speed ranges from 4 to 8 mm/s at a laser power of 1500–1900 W. The optimal scanning speed ranges from 6 to 10 mm/s at a laser power of 2200–2600 W. This process window serves as a preset parameter benchmark for ensuring part forming quality. However, process instabilities can still compromise high-quality fabrication, even when using pre-optimized parameters. Therefore, real-time monitoring and closed-loop control of process parameters during printing are of paramount importance.

Establishing quantitative relationships among process parameters, multi-source signals, and forming quality is a crucial prerequisite for implementing multi-sensor-based process monitoring. Fig. 20 systematically elucidates the interconnections between process parameters, multi-source signal features, and forming quality scores in the L-DED process. Statistical results clearly reveal a piecewise linear relationship between signal feature values and laser power at a fixed scanning speed. For instance, at a scanning speed of 2 mm/s and laser power of 600 W, the single-bead forming quality is optimal, with corresponding VA value of 1.72×10^4 pixels. At a scanning speed of 4 mm/s and laser power of 900–1700 W, the single-bead forming quality is optimal, with a corresponding VA value range of 1.95×10^4-3.14×10^4 pixels. At a scanning speed of 6 mm/s and laser power of 1500–2300 W, the single-bead forming quality is optimal, with a corresponding visible image area feature value range of approximately 2.4×10^4-3.67×10^4 pixels.

Therefore, the effective ranges of the corresponding signal features

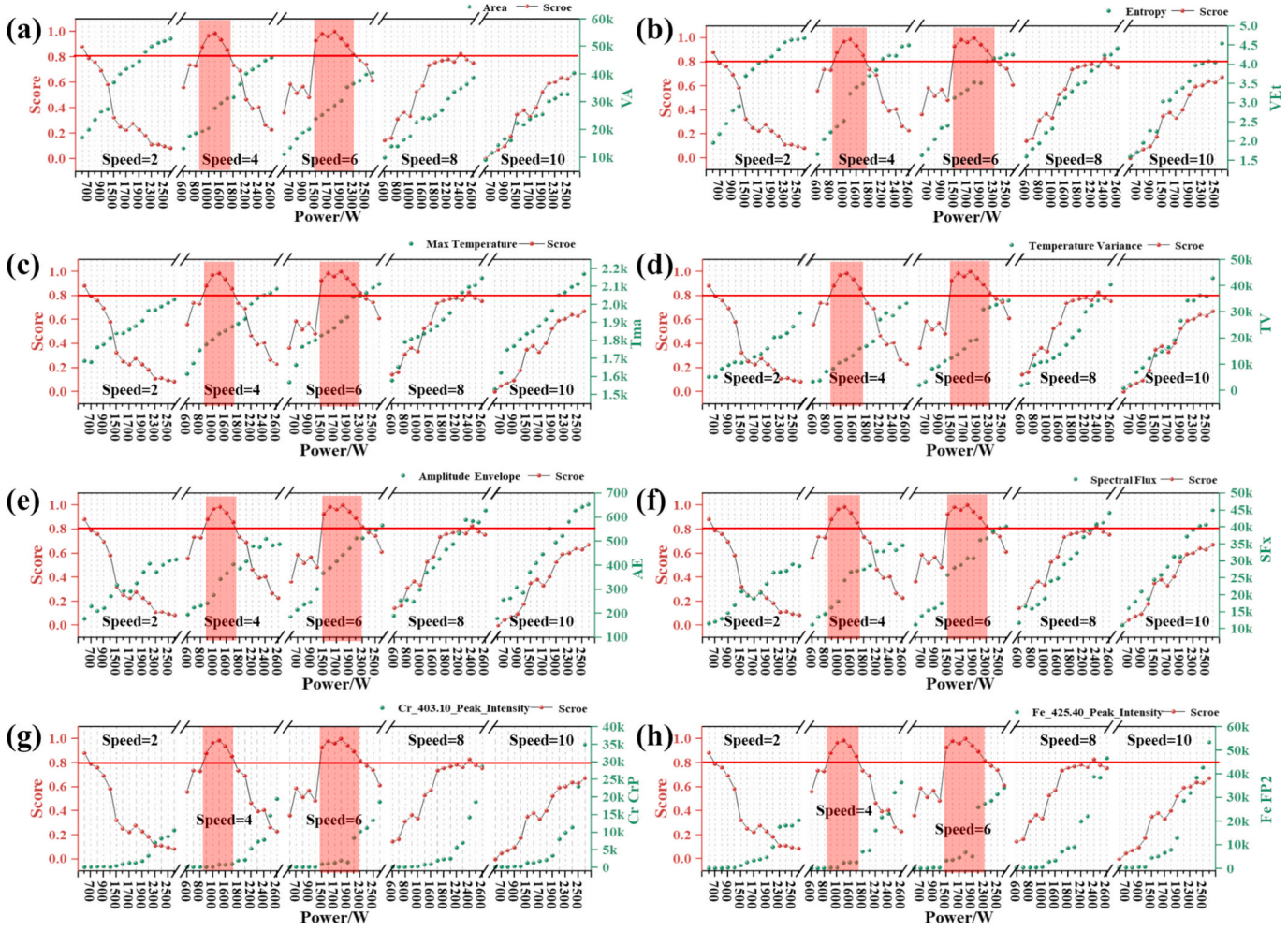

Fig. 20. Statistical results of process parameters – multi-source signals – forming quality: (a) Area; (b) Entropy; (c) Max temperature; (d) Temperature variance; (e) Amplitude envelop; (f) Spectral flux; (g) Cr peak intensity; (h) Fe peak intensity.

Table 10
Signal feature ranges in optimized processes.

Process Parameters		Reasonable Ranges of Multi-Source Signal Feature Values(k = $\times 10^3$)								Forming Quality
Scan speed (mm/s)	Power (kW)	VA (kpix)	VEt	Tma (k℃)	TV (k)	AE	SFx (k)	CrP (k)	FP2 (k)	Score(>0.8)
2	0.6	17.2	1.95	1.69	5.3	177	11.6	0.15	0.14	0.88
4	0.9–1.7	19.5–31.4	2.4–3.5	1.8–1.88	8.5–16.1	240–400	16.2–27.2	0.2–0.95	0.35–2.8	0.86–0.99
6	1.5–2.3	24–36.7	3.1–4.2	1.83–2.05	12.6–31.8	370–510	25.9–36.7	0.1–10.3	3.5–27.8	0.82–1

differ across processing regimes. This implies that for process monitoring, appropriate multi-source signal feature windows must be matched to different process parameter sets. During monitoring, if a signal feature value falls outside its designated window, it indicates an anomaly in the process parameters, necessitating corrective feedback control. Table 10 summarizes the distribution ranges of multi-source signal features under different laser powers and scanning speeds, along with the corresponding single-bead forming quality scores. This table will provide essential prior knowledge and a foundational database for upcoming multi-sensor feature fusion-based process monitoring and closed-loop control strategies.

Although individual signal features exhibit similar monotonic trends with process parameters at the macro-level, their synergistic value lies in anomaly detection: different defect types selectively excite distinct sensors (e.g., porosity triggers acoustic transients while powder inconsistencies manifest in CMOS morphology), and cross-modal verification reduces false alarm rates by distinguishing genuine anomalies from sensor-specific noise.

5. Conclusion

This work presented a methodology based on multi-sensor signal perception and spatiotemporal feature fusion, enabling in-situ comprehensive analysis of melt pool evolution and deep mining of process data in L-DED. A robot-assisted in-situ monitoring system integrating visual, infrared, acoustic, and spectral sensors was developed, achieving synchronous online acquisition of visible-light images, thermal images, acoustic signals, and plasma spectra. Spatiotemporal feature fusion of these heterogeneous data streams was realized by converting melt and thermal images from spatial pixel data into time-series feature signals. Key signal features characterizing melt pool geometric morphology, temperature distribution, reaction intensity, and element excitation state were identified while redundant features were discarded out using correlation analysis. A systematic investigation of the intrinsic relationships between process parameters and these key signal features elucidated how laser power and scanning speed govern melt pool dynamic behavior. Stable L-DED process windows were then established by examining the effects of process parameters on forming quality. The resulting L-DED process windows were identified as optimal scanning speed ranges of 2–6 mm/s at 600–1000 W, 4–8 mm/s at 1500–1900 W, and 6–10 mm/s at 2200–2600 W. Based on these results, a quantitative mapping among process parameters, multi-modal signals, and forming quality was constructed, and reasonable value ranges for each characteristic signal were determined. This research provides critical prior knowledge and data-driven support for online monitoring and closed-loop control of the L-DED process. It contributes to a paradigm shift from post-process defect detection to real-time defect prevention, offering an effective pathway to improve process stability and part quality consistency in metal additive manufacturing.

Future work will focus on integrating the established multi-dimensional signal-feature windows into a real-time closed-loop controller for online defect suppression. Multimodal deep learning architectures will be further investigated to exploit the complementary information across the four sensing modalities for high-precision defect classification and localization.

CRediT authorship contribution statement

Gen Tian: Writing – review & editing, Writing – original draft, Methodology, Investigation, Data curation. **Yang Zhao:** Writing – review & editing, Methodology, Investigation. **Wenyu Wang:** Validation, Investigation. **Guofeng Han:** Formal analysis. **Zhiqiang Ren:** Validation, Resources. **Xiaoming Wang:** Writing – review & editing, Supervision, Conceptualization. **Lu Lu:** Writing – review & editing, Writing – original draft, Supervision, Resources, Conceptualization. **Sheng Zhu:** Supervision, Funding acquisition, Conceptualization.

Declaration of competing interest

The authors declare that they have no known competing financial interests or personal relationships that could have appeared to influence the work reported in this paper.

Acknowledgement

This work was supported by National Key Research and Development Program of China, grant number 2022YFF0609000.

Appendix A. Supplementary data

Supplementary data to this article can be found online at https://doi.org/10.1016/j.matdes.2026.115924.

Data availability

Data will be made available on request.

References

[1] R. Liu, H. Yang, Multimodal probabilistic modeling of melt pool geometry variations in additive manufacturing, Addit. Manuf. 61 (2023) 103375.
[2] L. Chen, G. Bi, X. Yao, J. Su, C. Tan, W. Feng, M. Benakis, Y. Chew, S.K. Moon, In-situ process monitoring and adaptive quality enhancement in laser additive manufacturing: a critical review, J. Manuf. Syst. 74 (2024) 527–574.
[3] H. Li, L. Hu, J. Ye, W. Wei, X. Gao, Z. Qian, Y. Long, A high-precision in-situ monitoring system for laser directed energy deposition melt pool 3D morphology based on deep learning, J. Intell. Manuf. 1–20 (2024).
[4] L. Gao, A.C. Chuang, P. Kenesei, Z. Ren, L. Balderson, T. Sun, An operando synchrotron study on the effect of wire melting state on solidification microstructures of Inconel 718 in wire-laser directed energy deposition, Int. J. Mach. Tool Manuf. 194 (2024) 104089.
[5] S. Sharma, K.M. Krishna, S.S. Joshi, M. Radhakrishnan, S. Palaniappan, S. Dussa, R. Banerjee, N.B. Dahotre, Laser based additive manufacturing of tungsten: multi-scale thermo-kinetic and thermo-mechanical computational model and experiments, Acta Mater. 259 (2023) 119244.
[6] J.C. Haley, J.M. Schoenung, E.J. Lavernia, Observations of particle-melt pool impact events in directed energy deposition, Addit. Manuf. 22 (2018) 368–374.
[7] C.L.A. Leung, S. Marussi, R.C. Atwood, M. Towrie, P.J. Withers, P.D. Lee, In situ X-ray imaging of defect and molten pool dynamics in laser additive manufacturing, Nat. Commun. 9 (1) (2018) 1355.
[8] M. Perani, S. Baraldo, M. Decker, A. Vandone, A. Valente, B. Paoli, Track geometry prediction for Laser Metal Deposition based on on-line artificial vision and deep neural networks, Robot. Comput.-Integr. Manuf. 79 (2023) 8.
[9] S. Oster, P.P. Breese, A. Ulbricht, G. Mohr, S.J. Altenburg, A deep learning framework for defect prediction based on thermographic in-situ monitoring in laser powder bed fusion, J. Intell. Manuf. 20 (2023).
[10] L. Chen, X. Yao, C. Tan, W. He, J. Su, F. Weng, Y. Chew, N.P.H. Ng, S.K. Moon, In-situ crack and keyhole pore detection in laser directed energy deposition through acoustic signal and deep learning, Addit. Manuf. 69 (2023).

[11] L. Chen, X. Yao, S.K. Moon, In-situ acoustic monitoring of direct energy deposition process with deep learning-assisted signal denoising, Materials Today: Proceedings 70 (2022) 136–142.
[12] B. Squires, D. Flannery, T. Bivens, R. Banerjee, B. McWilliams, K. Cho, A. Neogi, N. B. Dahotre, A.A. Voevodin, Laser-Induced Breakdown Spectroscopy for composition monitoring during directed energy deposition of graded Fe-Ni alloys, Int. J. Adv. Manuf. Technol. 132 (7) (2024) 3877–3888.
[13] L. Chen, S.K. Moon, In-situ defect detection in laser-directed energy deposition with machine learning and multi-sensor fusion, J. Mech. Sci. Technol. 38 (9) (2024) 4477–4484.
[14] L. Chen, X. Yao, W. Feng, Y. Chew, S.K. Moon, Multimodal sensor fusion for real-time location-dependent defect detection in laser-directed energy deposition, arXiv preprint arXiv:2305.13596 (2023).
[15] L. Kong, X. Peng, Y. Chen, P. Wang, M. Xu, Multi-sensor measurement and data fusion technology for manufacturing process monitoring: a literature review, Int. J. Extreme Manuf. 2 (2) (2020) 022001.
[16] B. Shen, J. Lu, Y.M. Wang, D.L. Chen, J. Han, Y. Zhang, Z. Zhao, Multimodal-based weld reinforcement monitoring system for wire arc additive manufacturing, J. Mater. Res. Technol-JMRT 20 (2022) 561–571.
[17] Q. Wu, F. Yang, C. Lv, C. Liu, W. Tang, J. Yang, In-situ quality intelligent classification of additively manufactured parts using a multi-sensor fusion based melt pool monitoring system, Additive Manufacturing Frontiers 3 (3) (2024) 200153.
[18] A. Gaikwad, R.J. Williams, H. de Winton, B.D. Bevans, Z. Smoqi, P. Rao, P. A. Hooper, Multi phenomena melt pool sensor data fusion for enhanced process monitoring of laser powder bed fusion additive manufacturing, Mater. Des. 221 (2022) 22.
[19] M. Montazeri, A.R. Nassar, C.B. Stutzman, P. Rao, Heterogeneous sensor-based condition monitoring in directed energy deposition, Addit. Manuf. 30 (2019) 10.
[20] L. Chen, G. Bi, X. Yao, C. Tan, J. Su, N.P.H. Ng, Y. Chew, K. Liu, S.K. Moon, Multisensor fusion-based digital twin for localized quality prediction in robotic laser-directed energy deposition, Robot. Comput.-Integr. Manuf. 84 (2023).
[21] A. Shrivastava, S. Mukherjee, S.S. Chakraborty, Addressing the challenges in remanufacturing by laser-based material deposition techniques, Opt. Laser Technol. 144 (2021) 107404.
[22] J. Powell, D. Koti, X. Garmendia, K. Voisey, Assessing the quality and productivity of laser cladding and direct energy deposition: guidelines for researchers, J. Laser Appl. 35 (1) (2023).
[23] E.S. Gedraite, M. Hadad, Investigation on the effect of a Gaussian Blur in image filtering and segmentation, Proceedings ELMAR-2011, IEEE (2011) 393–396.
[24] A.M. Reza, Realization of the contrast limited adaptive histogram equalization (CLAHE) for real-time image enhancement, Journal of VLSI Signal Processing Systems for Signal, Image and Video Technology 38 (2004) 35–44.
[25] M. Bobyr, V. Dobritsa, A. Sizov, A. Dorodnykh, Ontological model for creating object contours in an image, Autom. Doc. Math. Ling. 59 (Suppl 2) (2025) S138–S144.
[26] Z. Kulpa, Area and perimeter measurement of blobs in discrete binary pictures, Comput. Graphics Image Process. 6 (5) (1977) 434–451.
[27] H. Gaja, F. Liou, Defects monitoring of laser metal deposition using acoustic emission sensor, Int. J. Adv. Manuf. Technol. 90 (2017) 561–574.
[28] Z. Bai, Z. Li, Z. Zhang, R. Qin, S. Zhang, Y. Xu, G. wen,of the china welding institution,, On-line monitoring of TIG welding quality of nuclear power plug tube based on arc spectrum, Transactions 45 (5) (2024) 8–19.
[29] S. Waqar, H.M. Khan, A. Nazir, C. Chen, U.W. Qazi, H. Ejaz, Thermal Variables evolution inside melt pool during lpbf of 316l stainless steel: a numerical approach, Additive Manufacturing Frontiers (2025) 200236.
[30] Y. Zhang, B. Chen, C. Tan, X. Song, H. Zhao, Investigation of keyhole behaviour and its impact on the performance of laser beam oscillating welding through imaging and acoustic signal analysis, Sci. Technol. Weld. Join. 28 (9) (2023) 1003–1010.
[31] C. Zhao, N.D. Parab, X.X. Li, K. Fezzaa, W.D. Tan, A.D. Rollett, T. Sun, Critical instability at moving keyhole tip generates porosity in laser melting, Science 370 (6520) (2020) 1080–1086.
[32] K. Zhang, Y. Chen, S. Marussi, X. Fan, M. Fitzpatrick, S. Bhagavath, M. Majkut, B. Lukic, K. Jakata, A. Rack, Pore evolution mechanisms during directed energy deposition additive manufacturing, Nat. Commun. 15 (1) (2024) 1715.
[33] M. Hamidi Nasab, G. Masinelli, C. de Formanoir, L. Schlenger, S. Van Petegem, R. Esmaeilzadeh, K. Wasmer, A. Ganvir, A. Salminen, F. Aymanns, Harmonizing sound and light: X-ray imaging unveils acoustic signatures of stochastic inter-regime instabilities during laser melting, Nat. Commun. 14 (1) (2023) 8008.
[34] W. Ren, J. Mazumder, In-situ porosity recognition for laser additive manufacturing of 7075-Al alloy using plasma emission spectroscopy, Sci. Rep. 10 (1) (2020) 19493.
[35] A. Gleizes, Y. Cressault, Effect of metal vapours on the radiation properties of thermal plasmas, Plasma Chem. Plasma Process. 37 (3) (2017) 581–600.
[36] H.R. Griem, Principles of plasma spectroscopy, Fast Electrical and Optical Measurements: Volume I—Current and Voltage Measurements/Volume II—Optical Measurements, Springer1986, pp. 885–910.
[37] W. Demtröder, Laser spectroscopy: basic concepts and instrumentation, NASA STI/Recon Technical Report A 82 (1981) 12273.
[38] M.A. Gigosos, V. Cardenoso, New plasma diagnosis tables of hydrogen Stark broadening including ion dynamics, J. Phys. B Atomic Mol. Phys. 29 (20) (1996) 4795.
[39] J.J. Olivero, R. Longbothum, Empirical fits to the Voigt line width: a brief review, J. Quant. Spectrosc. Radiat. Transf. 17 (2) (1977) 233–236.
[40] C. Aragón, J.A. Aguilera, Characterization of laser induced plasmas by optical emission spectroscopy: a review of experiments and methods, Spectrochim. Acta B At. Spectrosc. 63 (9) (2008) 893–916.
[41] N. Konjević, M. Ivković, S. Jovićević, Spectroscopic diagnostics of laser-induced plasmas, Spectrochim. Acta B At. Spectrosc. 65 (8) (2010) 593–602.